Neuron

Article

Rebuilding essential active zone functions within a synapse

Graphical abstract

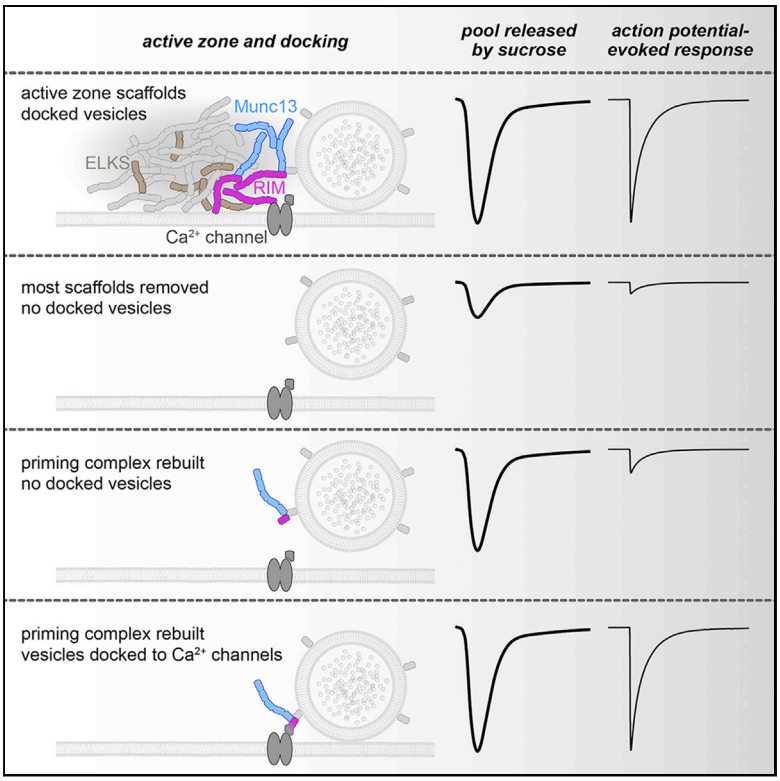

Highlights

- RIM + ELKS knockout disrupts active zones and vesicle docking, priming, and release
- RIM zinc fingers rescue fusion competence by recruiting Munc13 to undocked vesicles
- Linking RIM zinc fingers to $Ca_V\beta4$ restores docking and Ca^{2+} triggering of release
- This 80 kDa β4-Zn protein bypasses the need for megadalton-sized secretory machines

Authors

Chao Tan, Shan Shan H. Wang, Giovanni de Nola, Pascal S. Kaeser

Correspondence

kaeser@hms.harvard.edu

In brief

Presynaptic active zones are megadalton-sized protein machines for spatiotemporal precision of neurotransmitter release. Tan et al. ablate active zones and rebuild their functions within synapses using small protein domains. RIM zinc fingers rendered undocked vesicles fusion competent, and Ca^{2+} triggering of release was restored by tethering this priming domain to Ca^{2+} channels.

Tan et al., 2022, Neuron *110*, 1498–1515
May 4, 2022
https://doi.org/10.1016/j.neuron.2022.01.026

CellPress

CellPress

Neuron

Article

Rebuilding essential active zone functions within a synapse

Chao Tan,[1] Shan Shan H. Wang,[1] Giovanni de Nola,[1] and Pascal S. Kaeser[1,2,*]
[1]Department of Neurobiology, Harvard Medical School, Boston, MA 02115, USA
[2]Lead contact
*Correspondence: kaeser@hms.harvard.edu
https://doi.org/10.1016/j.neuron.2022.01.026

SUMMARY

Presynaptic active zones are molecular machines that control neurotransmitter secretion. They form sites for vesicle docking and priming and couple vesicles to Ca^{2+} entry for release triggering. The complexity of active zone machinery has made it challenging to determine its mechanisms in release. Simultaneous knockout of the active zone proteins RIM and ELKS disrupts active zone assembly, abolishes vesicle docking, and impairs release. We here rebuild docking, priming, and Ca^{2+} secretion coupling in these mutants without reinstating active zone networks. Re-expression of RIM zinc fingers recruited Munc13 to undocked vesicles and rendered the vesicles release competent. Action potential triggering of release was reconstituted by docking these primed vesicles to Ca^{2+} channels through attaching RIM zinc fingers to $Ca_V\beta4$-subunits. Our work identifies an 80-kDa β4-Zn protein that bypasses the need for megadalton-sized secretory machines, establishes that fusion competence and docking are mechanistically separable, and defines RIM zinc finger-Munc13 complexes as hubs for active zone function.

INTRODUCTION

Essential insight into the functioning of synaptic exocytotic machinery has come from rebuilding the fusion process *in vitro*. Reconstitution assays have revealed that the minimal machinery for Ca^{2+}-triggered exocytosis consists of SNARE proteins, Munc18, Munc13, and synaptotagmin (Hu et al., 2003; Ma et al., 2013; Tucker et al., 2004). However, fusion speed in these assays is orders of magnitude slower than at synapses, and spatial precision of exocytosis with its targeting toward postsynaptic receptor domains on target cells cannot be studied in these *in vitro* systems. These functions are carried out by the active zone, a molecular machine that is attached to the presynaptic plasma membrane and is composed of many megadalton-sized protein assemblies (Emperador-Melero and Kaeser, 2020; Südhof, 2012).

Central functions of the active zone are the generation of releasable vesicles and the positioning of these vesicles close to Ca^{2+} channels for rapid fusion-triggering (Augustin et al., 1999; Biederer et al., 2017; Deng et al., 2011; Imig et al., 2014; Kaeser et al., 2011; Liu et al., 2011). Active zones are composed of families of scaffolding proteins including RIM, ELKS (also called ERC, CAST, or Rab6IP2), Munc13, RIM-BP, Bassoon/Piccolo and Liprin-α (Südhof, 2012). Each protein family is encoded by multiple genes and the individual proteins are large, ranging from 120 to 420 kDa, forming complex protein networks. Understanding assembly mechanisms of these molecular machines remains a major challenge.

Gene knockout and related studies have uncovered loss-of-function phenotypes for individual active zone proteins. In essence, these studies established that each protein, in one way or another, participates in the control of each key exocytotic parameter. These parameters include (1) the docking of vesicles (defined morphologically: the physical attachment of vesicles to the target membrane as assessed by electron microscopy), (2) the priming of vesicles (defined functionally: the production of release-competent vesicles through enhancing their fusogenicity), and (3) the coupling of these vesicles to Ca^{2+} channels (defined functionally: the releasability of primed vesicles in response to an action potential as a function of the distance of the primed vesicles to the source of Ca^{2+} entry). For example, roles in vesicle docking and priming have been described for RIM (Calakos et al., 2004; Deng et al., 2011; Han et al., 2011; Kaeser et al., 2011; Koushika et al., 2001), Munc13 (Aravamudan et al., 1999; Augustin et al., 1999; Deng et al., 2011; Imig et al., 2014; Richmond et al., 1999), Liprin-α (Emperador-Melero et al., 2021; Spangler et al., 2013; Wong et al., 2018), ELKS (Dong et al., 2018; Held et al., 2016; Kawabe et al., 2017; Matkovic et al., 2013), Piccolo/Bassoon (Parthier et al., 2018), and RIM-BP (Brockmann et al., 2019). Similarly, the control of Ca^{2+} secretion coupling is mediated by the same proteins, with roles for RIM, RIM-BP, Bassoon, and ELKS (Acuna et al., 2015; Davydova et al., 2014; Dong et al., 2018; Grauel et al., 2016; Han et al., 2011; Kaeser et al., 2011; Kittel et al., 2006; Liu et al., 2014, 2011). A true mechanistic understanding of the active zone, however, has been difficult to achieve. This is in part because reconstitution assays, powerful for untangling mechanisms of the fusion reaction itself (Hu et al., 2003; Ma et al., 2013; Tucker et al., 2004), are not possible for the active zone due to its molecular complexity. Furthermore, the redundancy of scaffolding and

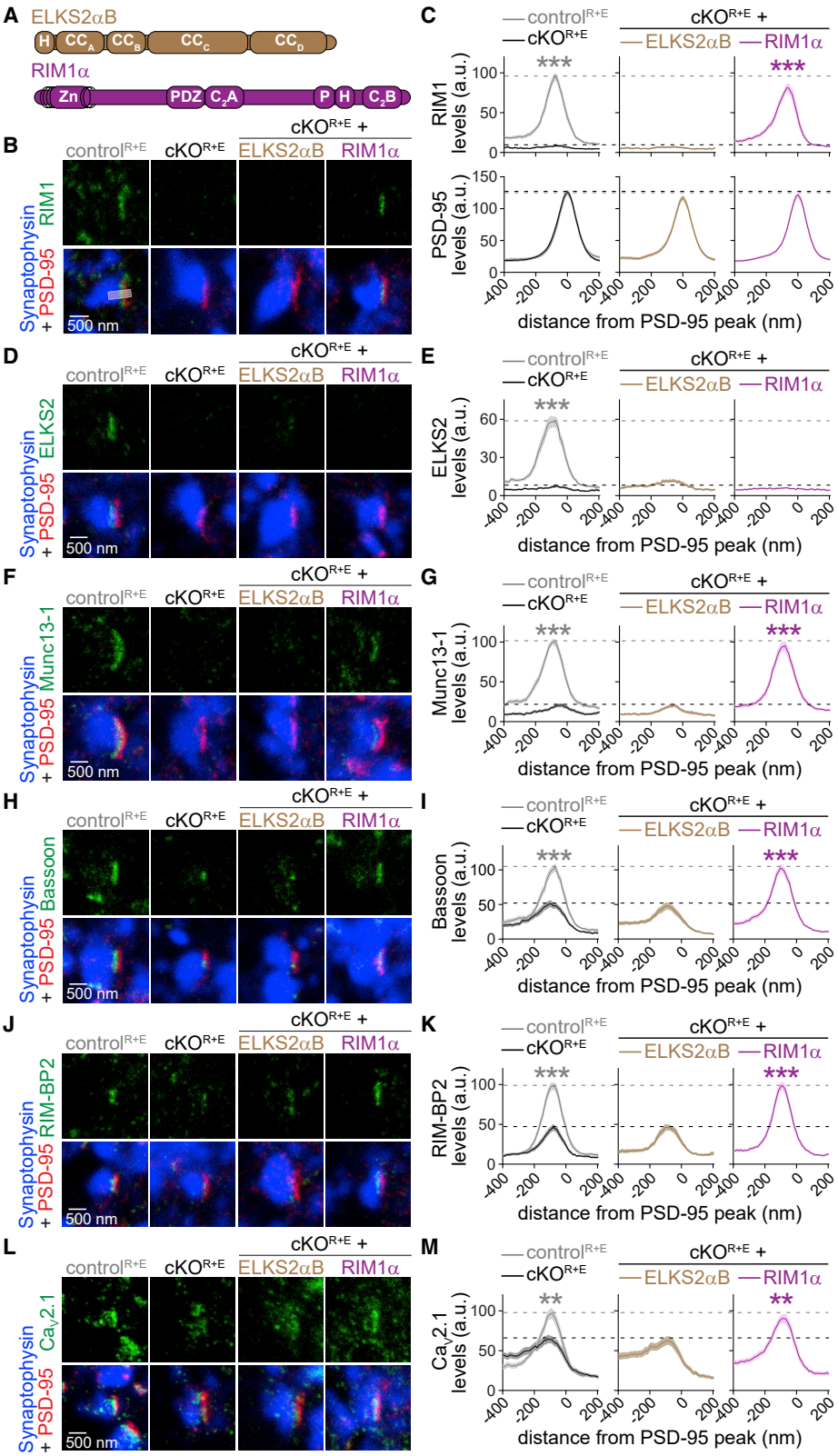

(legend on next page)

release mechanisms has made it challenging to distinguish effects on active zone assembly from those on active zone function. Ultimately, it has not been possible to define which of the many candidate mechanisms at the active zone suffice to drive fast, action potential-triggered release.

Simultaneous conditional knockout of RIM and ELKS leads to disassembly of the active zone with loss of RIM, ELKS, RIM-BP, Piccolo, Bassoon, and Munc13, a near-complete absence of vesicle docking, and a strong reduction in action potential-evoked exocytosis (Wang et al., 2016). General features of synaptic structure including the formation of boutons, the accumulation of vesicles, and the generation of synaptic contacts remain intact in these mutants. This has established that RIM and ELKS form a scaffolding complex that holds the active zone together.

Here, we use this active zone disruption through RIM + ELKS knockout to develop an approach for rebuilding hallmark functions of these secretory machines within synapses. Our overall goal was to develop a deep mechanistic understanding of active zone function and to define which of the many mechanisms are sufficient to drive release. We find that vesicles can be rendered release competent by re-expression of RIM zinc fingers, which positioned activated Munc13 on undocked vesicles. Docking of these vesicles next to Ca^{2+} channels was required to restore action potential triggering of release. We achieved this using a single artificial fusion protein consisting of the RIM zinc finger and the $Ca_V\beta4$ subunit, which resulted in recovery of fusion strength and speed after active zone disruption. These findings establish the minimal requirements for active zone function and define key protein domains sufficient to mediate these requirements.

RESULTS

RIM restores structure and function at synapses with disrupted active zones

We first used stimulated emission depletion (STED) superresolution microscopy to evaluate active zone disruption induced by conditional knockout of RIM and ELKS, which strongly impaired extent and precision of neurotransmitter release (Wang et al., 2016). Cultured hippocampal neurons with floxed alleles for RIM1, RIM2, ELKS1, and ELKS2 were infected with cre-expressing lentiviruses to generate knockout (cKO^{R+E}) neurons or with control viruses to generate $control^{R+E}$ neurons. We then used a previously established workflow (Held et al., 2020; de Jong et al., 2018; Nyitrai et al., 2020; Wong et al., 2018) to assess active zone structure at 15–19 days *in vitro* (DIV). We identified side-view synapses in immunostainings by an elongated postsynaptic density (PSD, marked by PSD-95, STED) that was aligned with the edge of a synaptic vesicle cloud (synaptophysin, confocal), and assessed localization of target proteins (STED) relative to these markers in line profiles (Figures S1A–S1D). The cKO^{R+E} synapses had disrupted active zones with near-complete loss of ELKS2, RIM1, and Munc13-1, and strong reductions in Bassoon and RIM-BP2 (Figures 1A–1K). In addition, we observed a partial loss of $Ca_V2.1$ (Figures 1L and 1M), the $\alpha1$-subunits of a major voltage-gated Ca^{2+} channel for release triggering at this synapse (Held et al., 2020). Removal of these active zone complexes, however, did not affect PSD-95 (Figure 1C) and led to increases in Liprin-$\alpha3$ (Figures S1E and S1F), a protein that connects active zone assembly pathways to structural plasticity (Emperador-Melero et al., 2021; Wong et al., 2018).

With the overall goal to rebuild active zone function using the minimally required protein domains and interactions, we first tested whether either RIM or ELKS mediate recovery of active zone structure and function on their own. We re-expressed RIM1α or ELKS2αB, the main synaptic isoforms of the corresponding gene families (Kaeser et al., 2009, 2011; Liu et al., 2014; Schoch et al., 2002; Wang et al., 1997), using lentiviruses (Figures 1A and S1G). We found that RIM1α was targeted correctly (Figures 1B and 1C) and was able to re-establish normal levels and active zone positioning of Munc13-1, Bassoon, RIM-BP2, $Ca_V2.1$, and Liprin-$\alpha3$ (Figures 1F–1M, S1E, and S1F). In contrast, re-expression of ELKS2αB did not lead to its localization to the target membrane area (Figures 1D and 1E) and did not restore the localization of other proteins (Figures 1F–1M, S1E, and S1F), even though it was expressed efficiently (Figure S1G). To assess protein levels upon rescue with an independent approach and to determine whether RIM-mediated active zone protein recruitment depends on RIM expression levels, we performed additional confocal microscopy experiments. Re-expression of lower or higher RIM1α levels using either a synapsin or ubiquitin promoter, respectively, mediated recovery of the other proteins dose dependently. Higher levels of RIM1α were driving the recruitment of higher levels of Munc13-1, $Ca_V2.1$, and RIM-BP2 (Figures S2A–S2F). Higher synaptic levels of RIM1α also resulted in higher active zone levels of RIM1α (Figures S2G and S2H). Altogether, these data indicate that RIM titrates levels of interacting proteins.

Figure 1. RIM re-expression restores active zone structure in RIM and ELKS knockout neurons

(A) Schematic of HA-tagged ELKS2αB and RIM1α, H, HA tag; CC, coiled-coil region; Zn, zinc finger domain; PDZ, PDZ domain; C_2A and C_2B, C_2 domains; P, proline rich (PxxP-) motif.

(B and C) Sample STED images (B) and quantification (C) of side-view synapses of cultured hippocampal neurons after knockout of RIM and ELKS (cKO^{R+E}; through expression of cre-lentiviruses in neurons of floxed mice) or in corresponding control neurons ($control^{R+E}$; expression of recombination-deficient cre in the same neurons) and in cKO^{R+E} neurons after lentiviral re-expression of ELKS2αB or RIM1α. Neurons were antibody stained for RIM1 (imaged in STED), PSD-95 (imaged in STED), and synaptophysin (imaged in confocal). Peak position and levels (C) were analyzed in line profiles (600 nm × 200 nm, gray-shaded area in B, for STED analysis workflow, see Figures S1A–S1D) positioned perpendicular to the center of elongated PSD-95 structure and aligned to the PSD-95 peak, dotted lines mark $control^{R+E}$ (gray) and cKO^{R+E} (black) levels for comparison, a.u.: arbitrary units, 60 synapses/3 cultures each.

(D–M) Same as (B and C), but for ELKS2 (D and E), Munc13-1 (F and G), Bassoon (H and I), RIM-BP2 (J and K) or $Ca_V2.1$ (L and M), 60/3 each. PSD-95 levels were assessed as in (C) and were similar in each condition.

Data are mean ± SEM; $^{**}p < 0.01$, $^{***}p < 0.001$ compared with cKO^{R+E} as determined by two-way ANOVA followed by Dunnett's multiple comparisons post hoc tests. For STED workflow, evaluation of Liprin-$\alpha3$ by STED, and assessment of rescue protein expression by western blotting, see Figure S1; for additional confocal and STED experiments, see Figure S2.

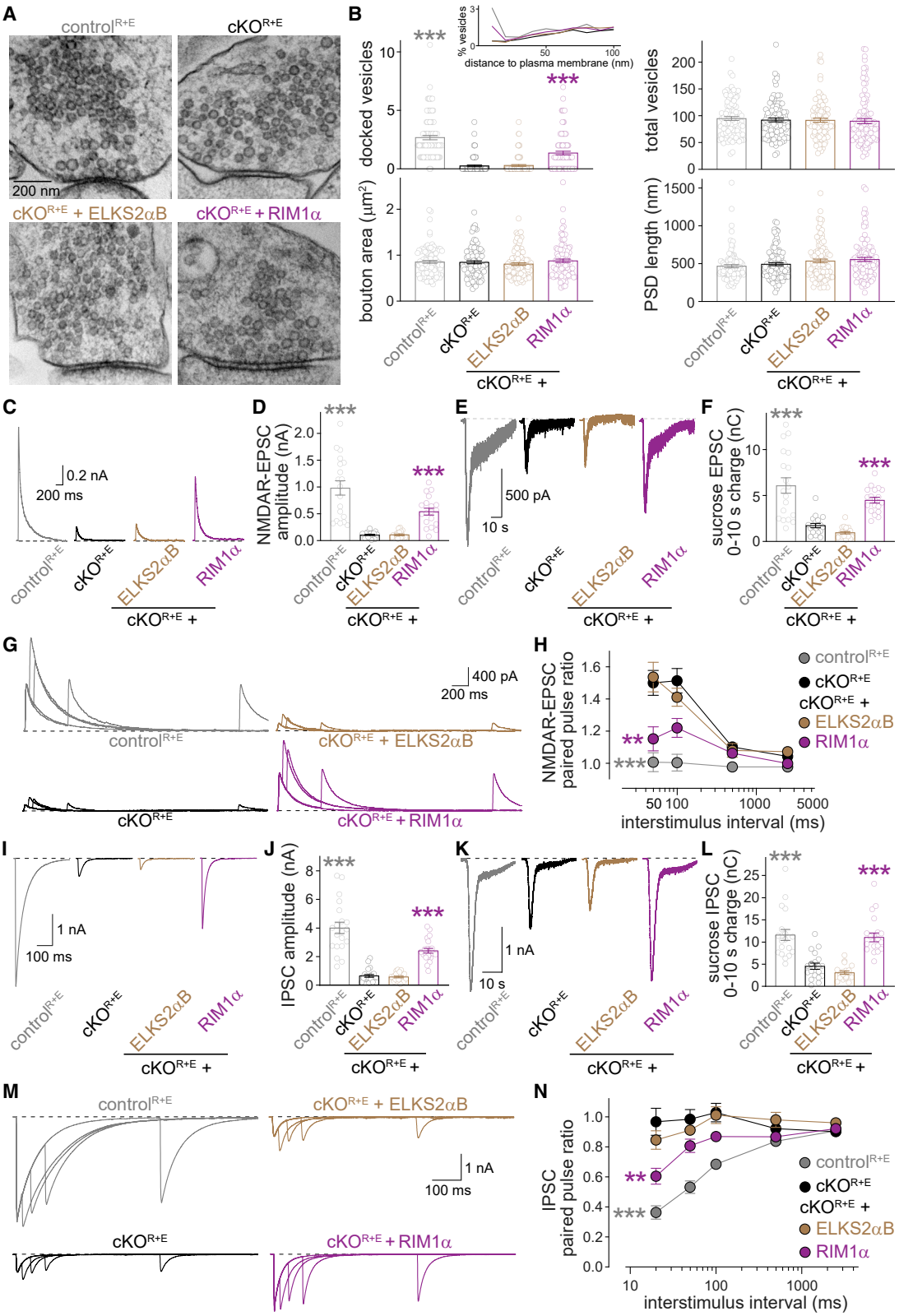

(legend on next page)

We next tested whether RIM1α re-expression restored key active zone functions, synaptic vesicle docking, and release (Figure 2). To assess synaptic ultrastructure, we fixed neurons with high-pressure freezing and analyzed electron microscopic images of synapses. Most cKO^{R+E} synapses lacked docked vesicles (assessed as vesicles for which the electron density of the vesicle membrane merges with that of the active zone target membrane), but other parameters including PSD length, bouton size, and total vesicle numbers were unaffected. RIM1α restored vesicle docking to 51% of its initial levels, while ELKS2αB expression did not improve docking (Figures 2A and 2B).

The active zone controls synaptic strength (sometimes also referred to as synaptic release probability), which is proportional to the product of the number of vesicles in the readily releasable pool (RRP) and the vesicular release probability p of each of these RRP vesicles. We measured synaptic strength and estimated these constituents, RRP and p, at excitatory and inhibitory synapses using electrophysiology (Figures 2C–2N). Vesicular release probability p is inversely correlated with the ratio of release in response to paired pulses at short interstimulus intervals (Zucker and Regehr, 2002), and application of hypertonic sucrose was used to estimate the RRP (Kaeser and Regehr, 2017; Rosenmund and Stevens, 1996). RIM1α mostly restored excitatory (Figures 2C–2H) and inhibitory (Figures 2I–2N) synaptic strength, and both RRP and p were recovered to a large extent at both synapse types. In contrast, ELKS2αB had no rescue activity on its own, consistent with the STED and electron microscopy data. Excitatory evoked transmission was monitored via NMDA receptors (NMDARs) in most experiments to avoid confounding effects of network activity triggered by AMPA receptor (AMPAR) activation. Decreasing initial p (by lowering extracellular Ca^{2+} or the use of low-affinity NMDAR antagonists) confirmed that paired pulse ratios provide an accurate estimate of changes in p as a consequence of genetic manipulations under our conditions (Figure S3). Together, these data establish that RIM is an important presynaptic organizer for the control of active zone protein levels, positioning, and function.

Re-expressed RIM zinc fingers localize to the synaptic vesicle cloud

For building a minimal recovery system, we next distinguished between RIM domains that mediate active zone targeting of RIM from those that are important for its functions in scaffolding other proteins and in mediating vesicle docking and release. We generated lentiviral constructs (Figures 3A and 3B) in which we either deleted individual RIM domains (RIM1-ΔZn, -ΔPDZ, -ΔC_2A, and -ΔC_2B) or that contained only one domain at a time (RIM1-Zn, -PDZ and -C_2B; the tested C_2A domain constructs were not efficiently expressed and hence C_2A domains could not be assessed in these experiments). cKO^{R+E} neurons were transduced with each individual virus for rescue, and each protein was expressed efficiently (Figures S4A and S4B).

Assessment of RIM active zone targeting using STED line profile analyses revealed that the PDZ domain was necessary for RIM target membrane localization after active zone disruption, as removing the PDZ domain abolished RIM active zone targeting (Figures 3C and 3D). Other domain deletions did not decrease RIM localization. Removing the C_2A domain slightly enhanced RIM active zone levels (Figure 3D). This could be because removing C_2A domains might enhance RIM expression, or because C_2A might suppress RIM active zone targeting. None of the tested single RIM domains was targeted to the plasma membrane opposed to the PSD (Figures 3E and 3F). Hence, while multiple RIM domains need to cooperate for RIM active zone targeting, the RIM PDZ domain is essential for such targeting. It is noteworthy that in neurons lacking only RIM, most active zone proteins remain localized to synapses, the PDZ domain is not essential for RIM localization to nerve terminals, and RIM1-ΔPDZ can enhance neurotransmitter release (de Jong et al., 2018; Kaeser et al., 2011). In active zone disrupted cKO^{R+E} synapses, this redundancy is lost and the PDZ domain is essential (Figures 3C and 3D). This loss of redundancy is further illustrated by the finding that RIM1α re-expression is not sufficient to restore all synaptic parameters, as docking and p are only partially recovered. Hence, the highly interconnected active zone protein networks rely on redundant scaffolding mechanisms that include ELKS (Held and Kaeser, 2018).

The RIM zinc finger alone, while not localized to active zones, was enriched within nerve terminals (Figures 3E and 3F). RIM1-Zn localization highly overlapped with the synaptic vesicle protein synaptophysin, suggesting that this domain may be associated with vesicles when expressed on its own. Since the RIM zinc finger interacts with the vesicular GTPases Rab3 and Rab27 (Dulubova et al., 2005; Fukuda, 2003; Wang et al., 1997), it is likely that RIM1-Zn associates through these interactions with synaptic vesicles. The complementary protein

Figure 2. RIM restores active zone functions in neurons with disrupted active zones

(A and B) Sample images (A) and analyses (B) of synapses of high-pressure-frozen neurons analyzed by electron microscopy. In (B), the number of docked vesicles per synapse profile is provided, and the inset shows vesicle distribution within 100 nm from the presynaptic plasma membrane in 10-nm bins. Quantification was performed on single sections, control^{R+E} 96 synapses/2 cultures, cKO^{R+E} 100/2, cKO^{R+E} + ELKS2αB 100/2, and cKO^{R+E} + RIM1α 98/2.

(C and D) Sample traces (C) and quantification (D) of EPSCs evoked by focal electrical stimulation and monitored via NMDARs, control^{R+E} 19 cells/3 cultures, cKO^{R+E} 18/3, cKO^{R+E} + ELKS2αB 18/3, and cKO^{R+E} + RIM1α 19/3.

(E and F) Sample traces (E) and quantification (F) of EPSCs triggered by hypertonic sucrose and monitored via AMPARs, the first 10 s were quantified to estimate the RRP, 19/3 each.

(G and H) Sample traces (G) and quantification (H) of EPSC paired pulse ratios monitored via NMDARs to estimate P, 16/3 each.

(I–N) As (C–H), but for electrically evoked IPSCs (I and J), sucrose-evoked IPSCs (K and L) and IPSC paired pulse ratios (M and N), J: control^{R+E} 20/3, cKO^{R+E} 21/3, cKO^{R+E} + ELKS2αB 21/3, and cKO^{R+E} + RIM1α 22/3; L: 19/3 each; N: 15/3 each.

Data are mean ± SEM; **p < 0.01, ***p < 0.001 compared with cKO^{R+E} as determined by Brown-Forsythe ANOVA followed by Games-Howell's multiple comparisons post hoc test (B, docked vesicles), Brown-Forsythe ANOVA followed by Dunnett's T3 multiple comparisons post hoc test (D), Kruskal-Wallis tests followed by Dunn's multiple comparisons post hoc tests (F, J, and L), or by two-way ANOVA followed by Dunnett's multiple comparisons post hoc tests (H and N). For analyses of NMDAR-EPSCs in low extracellular Ca^{2+} or with competitive NMDAR antagonists, see Figure S3.

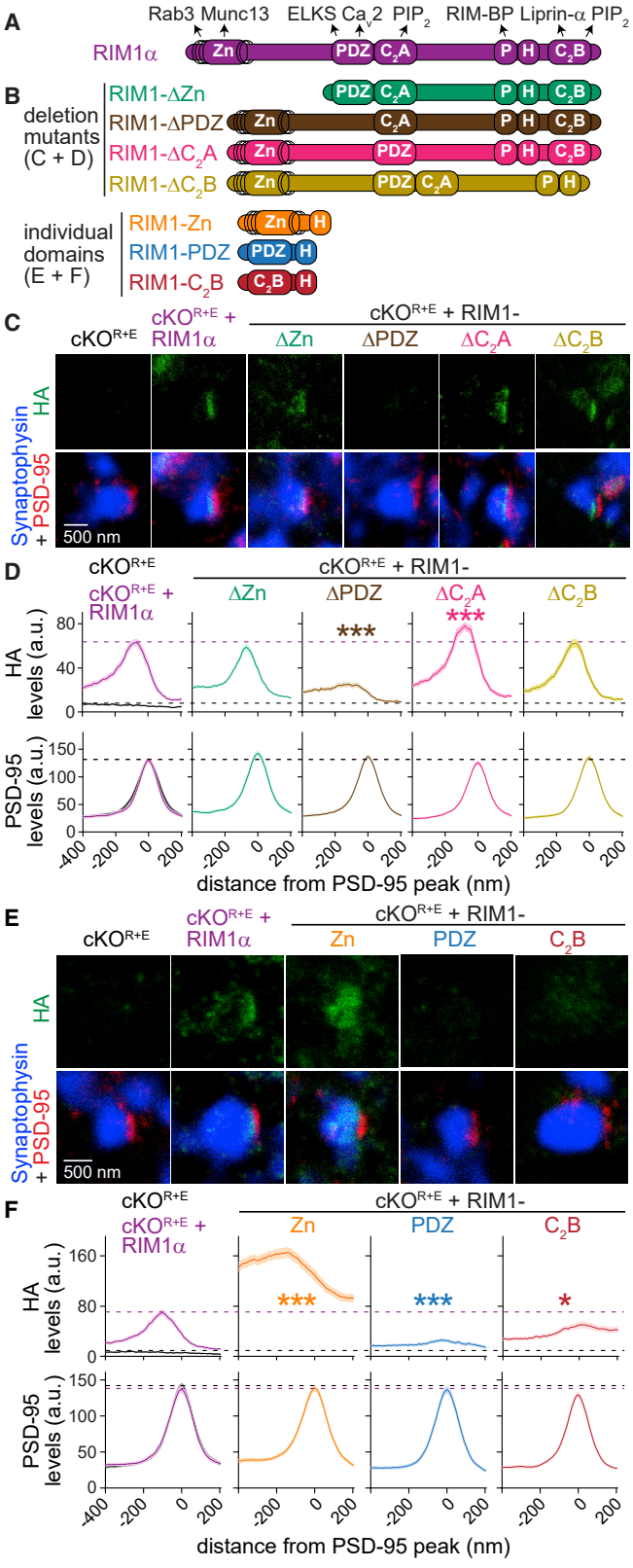

Figure 3. RIM PDZ domains mediate RIM active zone localization while zinc fingers associate with synaptic vesicles

(A) Schematic of RIM1α and of select presynaptic interactors.

(B) Schematic of RIM1 deletion mutants and individual domains used in (C–F).

(C and D) Sample STED images (C) and quantification (D) of side-view synapses stained for HA (STED), PSD-95 (STED), and synaptophysin (confocal), dotted lines mark cKO^{R+E} (black) and cKO^{R+E} + RIM1α (purple) levels for comparison, 60 synapses/3 cultures each.

(E and F) Same as (C and D), but for individual domains, 60/3 each.

Data are mean ± SEM; *p < 0.05, ***p < 0.001 compared with cKO^{R+E} + RIM1α as determined by two-way ANOVA followed by Dunnett's tests. For rescue expression analyses, see Figures S4A and S4B.

fragment, a version of RIM that lacks the zinc finger domain termed RIM1-ΔZn, localized to the active zone area apposed to the PSDs (Figures 3C and 3D), establishing that the zinc finger domain is not required for the synaptic delivery of RIM.

Re-expressed RIM zinc fingers recruit Munc13 to non-docked vesicles and enhance vesicle fusogenicity

The differential localization of RIM1-Zn (to vesicles) and RIM1-ΔZn (to the target membrane) may be related to their roles in release. Previous studies in RIM knockout synapses indicated that RIM zinc finger domains prime synaptic vesicles while the other domains tether Ca$_V$2 channels and interact with the target membrane for release triggering (Deng et al., 2011; de Jong et al., 2018; Kaeser et al., 2011). We tested these models by assessing the molecular roles (recruitment of Munc13 and Ca$_V$2s) and functional roles (priming, docking, and releasing of vesicles) of RIM1-Zn and RIM1-ΔZn after active zone disruption.

Strikingly, RIM1-Zn co-recruited Munc13 in a pattern mimicking the widespread localization of RIM1-Zn (Figures 4B and 4C). In contrast, RIM1-ΔZn, which contains the PDZ-, C$_2$A-, PxxP-, and C$_2$B-domains, localized to the active zone area (Figures 3A–3D) but was unable to enhance Ca$_V$2s or Munc13 (Figures 4A–4E). This suggests that RIM1-Zn, which binds to Munc13 and Rab3 (Betz et al., 2001; Dulubova et al., 2005), recruits Munc13 to synapses, stabilizes it, and turns it into a protein associated with synaptic vesicles. We next analyzed high-pressure-frozen neurons using electron microscopy from the same rescue conditions. Both RIM1-Zn and RIM1-ΔZn lacked docking activity, and synaptic vesicles remained undocked (Figures 4F and 4G). In conclusion, Munc13, a protein important for synaptic vesicle docking (Imig et al., 2014; Siksou et al., 2009), was not targeted to the presynaptic plasma membrane upon RIM1-Zn re-expression but was instead associated with the vesicle cloud. Recovering its presence in the nerve terminal was not sufficient to mediate docking.

Electrophysiological recordings revealed that RIM1-Zn and RIM1-ΔZn failed to restore action potential-triggered synaptic transmission and p at excitatory cKO^{R+E} synapses (Figures 4H–4M), and only some rescue of these parameters was observed at inhibitory cKO^{R+E} synapses (Figures S4C–S4H). This is different from rescue experiments after RIM knockout only (instead of cKO^{R+E}), where RIM1-ΔZn expression restores Ca^{2+} entry and mediates an increase in p (Deng et al., 2011; Kaeser et al., 2011). Hence, RIM C-terminal scaffolding domains need ELKS or N-terminal RIM sequences (Figures 1 and 2) to

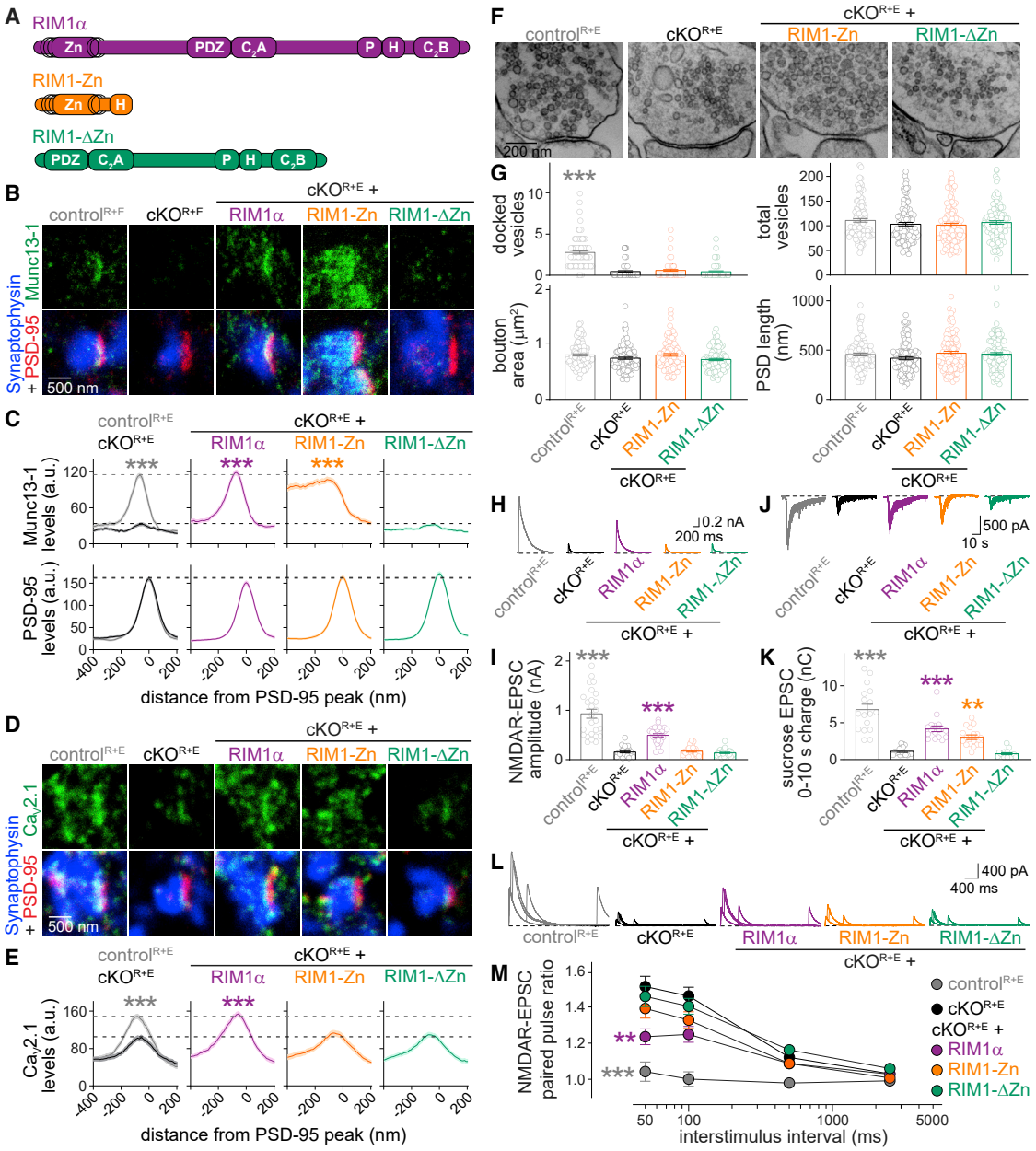

Figure 4. RIM zinc finger re-expression enhances fusogenicity of undocked vesicles through Munc13 recruitment

(A) Schematic of rescue proteins.

(B and C) Sample STED images (B) and quantification (C) of side-view synapses stained for Munc13-1 (STED), PSD-95 (STED), and synaptophysin (confocal), dotted lines mark control^{R+E} (gray) and cKO^{R+E} (black) levels for comparison, 60 synapses/3 cultures each.

(D and E) Same as (B and C), but for $Ca_V2.1$, 60/3 each. PSD-95 levels were similar across conditions, but are not shown for simplicity.

(F and G) Sample electron microscopic images (F) and analyses (G) of synapses of high-pressure-frozen neurons, control^{R+E} 105 synapses/2 cultures, cKO^{R+E} 110/2, cKO^{R+E} + RIM1-Zn 105/2, and cKO^{R+E} + RIM1-ΔZn 102/2.

(H and I) Sample traces (H) and quantification (I) of EPSCs evoked by focal electrical stimulation, 26 cells/4 cultures each.

(J and K) Sample traces (J) and quantification (K) of EPSCs triggered by hypertonic sucrose, 17/3 each.

(L and M) Sample traces (L) and quantification (M) of paired pulse ratios, 25/4 each.

Data are mean ± SEM; $^{**}p < 0.01$, $^{***}p < 0.001$ compared with cKO^{R+E} as determined by two-way ANOVA followed by Dunnett's tests (C, E, and M), Brown-Forsythe ANOVA followed by Games-Howell's multiple comparisons post hoc test (G, docked vesicles), or by Kruskal-Wallis tests followed by Dunn's multiple comparisons post hoc tests (I and K). For recordings of IPSCs, see Figures S4C–S4H.

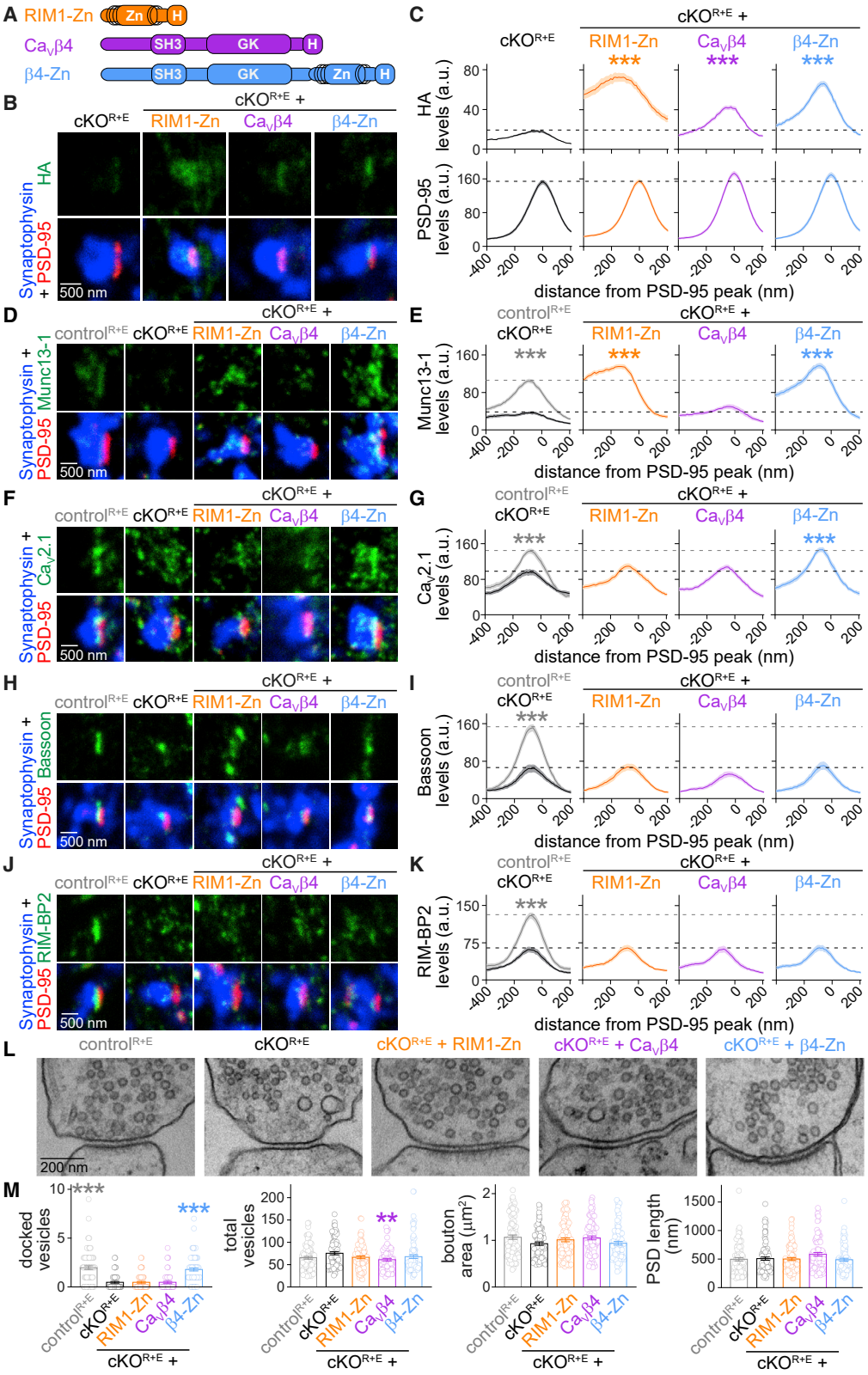

(legend on next page)

execute their roles in release, but are sufficient to mediate target membrane localization of RIM (Figures 3C and 3D).

RIM1-Zn, however, enhanced vesicle fusogenicity measured via application of hypertonic sucrose nearly as efficiently as full-length RIM1α (Figures 4J, 4K, S4E, and S4F). These data support the model that RIM zinc fingers activate Munc13 for vesicle priming by recruiting and monomerizing it via binding to Munc13 C_2A domains (Camacho et al., 2017; Deng et al., 2011) and—strikingly—this function can be executed on non-docked vesicles distant from the target membrane. These vesicles, however, were not accessible for efficient action potential triggering. We conclude that undocked vesicles can become release competent by positioning activated Munc13 on them. Hence, Munc13 enhances fusogenicity even if it is not localized to release sites at the target membrane, and these "molecularly" primed vesicles do not need to be docked. This may explain why some priming remains when the active zone is disrupted and docking is abolished (Wang et al., 2016), as some Munc13 may be recruited to vesicles via direct interactions (Quade et al., 2019).

Docking of release-competent vesicles to Ca^{2+} channels restores fast release in the absence of active zone scaffolds

With the goal to selectively rebuild active zone mechanisms without restoring the vast scaffolding structure, we aimed at positioning the release-competent vesicles close to Ca^{2+} entry. We screened eight fusion proteins of the RIM zinc finger domain to other proteins or protein fragments associated with the target membrane (Figure S5A). Fusions with $Ca_V\beta$ Ca^{2+} channel subunits appeared to restore evoked transmission and release probability (Figures S5B–S5E), suggesting that they may do so by co-localizing vesicle priming and Ca^{2+} entry. We selected the fusion of the RIM1 zinc finger to $Ca_V\beta4$ (Figure 5A, β4-Zn) for a full characterization because of its strong tendency to rescue. Endogenous $Ca_V\beta4$ is localized to active zones (Figures S5F and S5G), and HA-tagged $Ca_V\beta4$ requires Ca_V2 channels for its active zone localization (Figures S5H–S5K). β4-Zn was efficiently expressed (Figure S5L) and concentrated in an elongated structure at the target membrane (Figures 5A–5C). The β4-Zn protein recruited Munc13-1 to the target membrane (Figures 5D and 5E) and also enhanced $Ca_V2.1$ active zone levels back to control levels (Figures 5F and 5G). The effects on $Ca_V2.1$ were absent when $Ca_V\beta4$ or RIM1-Zn were expressed on their own. Importantly, β4-Zn did not restore levels of the active zone scaffolds Bassoon and RIM-BP2 (Figures 5H–5K). Hence, the $Ca_V\beta4$-fusion targets the priming complex of the RIM zinc finger and Munc13 to Ca^{2+} channels in the absence of megadalton-sized scaffolding networks that consist of full-length RIM, ELKS, RIM-BP, and Bassoon.

When we assessed these synapses using electron microscopy, we found that β4-Zn fully restored synaptic vesicle docking (Figures 5L and 5M), and the rescue efficacy appeared more robust than that of full-length RIM1α (Figures 2A and 2B). $Ca_V\beta4$ or RIM1-Zn alone did not enhance docking (Figures 5L and 5M). In electrophysiological recordings, we detected a full recovery of excitatory synaptic transmission, measured either via NMDARs (Figures 6A and 6B) or via AMPARs (Figures 6C and 6D), and of inhibitory synaptic transmission (Figures 6K and 6L). This included restoration of RRP (Figures 6E, 6F, 6M, and 6N) and p (Figures 6I, 6J, 6O, and 6P) back to levels indistinguishable from $control^{R+E}$ neurons. We next recorded an array of additional parameters which are affected by RIM + ELKS knockout, including miniature excitatory postsynaptic currents (mEPSCs), the extracellular Ca^{2+}-dependence of release, its sensitivity to the slow Ca^{2+} buffer EGTA, and pool sizes in response to 250, 500, or 1,000 mM sucrose. In cKO^{R+E} neurons, mEPSC frequencies decreased and mEPSC rise times increased, but amplitudes and decay times remained unchanged (Figures 6G, 6H, and S6A–S6D). The finding that mEPSC amplitudes are not increased indicates that postsynaptic homeostatic adaptations are not induced in these mutants, similar to other knockouts with strong decreases in release (He et al., 2017; Held et al., 2020; Schoch et al., 2001). β4-Zn fully restored mEPSC frequencies and rise times back to $control^{R+E}$ levels (Figures 6G, 6H, and S6C). β4-Zn also rescued the extracellular Ca^{2+} dependence (Figures S6E–S6G) and EGTA sensitivity (Figures S6H and S6I) of evoked release, and the response to various sucrose concentrations (Figures S6J and S6K). Altogether, these data establish that functional defects induced by active zone disruption are fully restored by β4-Zn expression. β4-Zn recruits Munc13 and mediates vesicle docking close to Ca^{2+} channels for recovery of extent and temporal precision of release. $Ca_V\beta4$ or RIM1-Zn alone did not mediate these functions except for RRP recovery by RIM1-Zn (Figures 4, 6, and S4), and it is hence unlikely that β4-Zn rescue activity is due to enhancement of Ca^{2+} entry or RRP through β-subunits directly (Dolphin, 2012; Guzman et al., 2019). In summary, these data establish that vesicle docking close to Ca^{2+} channels enhances p of vesicles that are primed by RIM1-Zn and Munc13.

To test the overall model that β4-Zn restores synaptic strength through docking of release-competent vesicles close to Ca^{2+}

Figure 5. A $Ca_V\beta4$-RIM zinc finger fusion protein recruits priming machinery close to Ca^{2+} channels and reconstitutes vesicle docking

(A) Schematic of rescue proteins. SH3, SRC homology domain 3; GK, guanylate kinase domain.

(B and C) Sample STED images (B) and quantification (C) of side-view synapses stained for HA (STED), PSD-95 (STED), and synaptophysin (confocal), dotted lines mark cKO^{R+E} (black) levels for comparison, 60 synapses/3 cultures each.

(D–K) Same as (B and C), but for Munc13-1 (D and E), $Ca_V2.1$ (F and G), Bassoon (H and I), and RIM-BP2 (J and K), 60/3 each. PSD-95 levels were similar across conditions but are not shown for simplicity, dotted lines mark $control^{R+E}$ (gray) and cKO^{R+E} (black) levels for comparison.

(L and M) Sample electron microscopic images (L) and analyses (M) of synapses of high-pressure-frozen neurons, $control^{R+E}$ 83 synapses/2 cultures, cKO^{R+E} 85/2, cKO^{R+E} + RIM1-Zn 84/2, cKO^{R+E} + $Ca_V\beta4$ 83/2, and cKO^{R+E} + β4-Zn 87/2.

Data are mean ± SEM; $^{**}p < 0.01$, $^{***}p < 0.001$ compared with cKO^{R+E} as determined by two-way ANOVA followed by Dunnett's tests (C, E, G, I, and K), Brown-Forsythe ANOVA followed by Games-Howell's multiple comparisons post hoc test (M, docked vesicles), or by one-way ANOVA followed by Dunnett's multiple comparisons post hoc tests (M, total vesicles). For assessment of various rescue fusion proteins, STED analyses of Cavβ4, and expression level analyses of rescue proteins, see Figure S5.

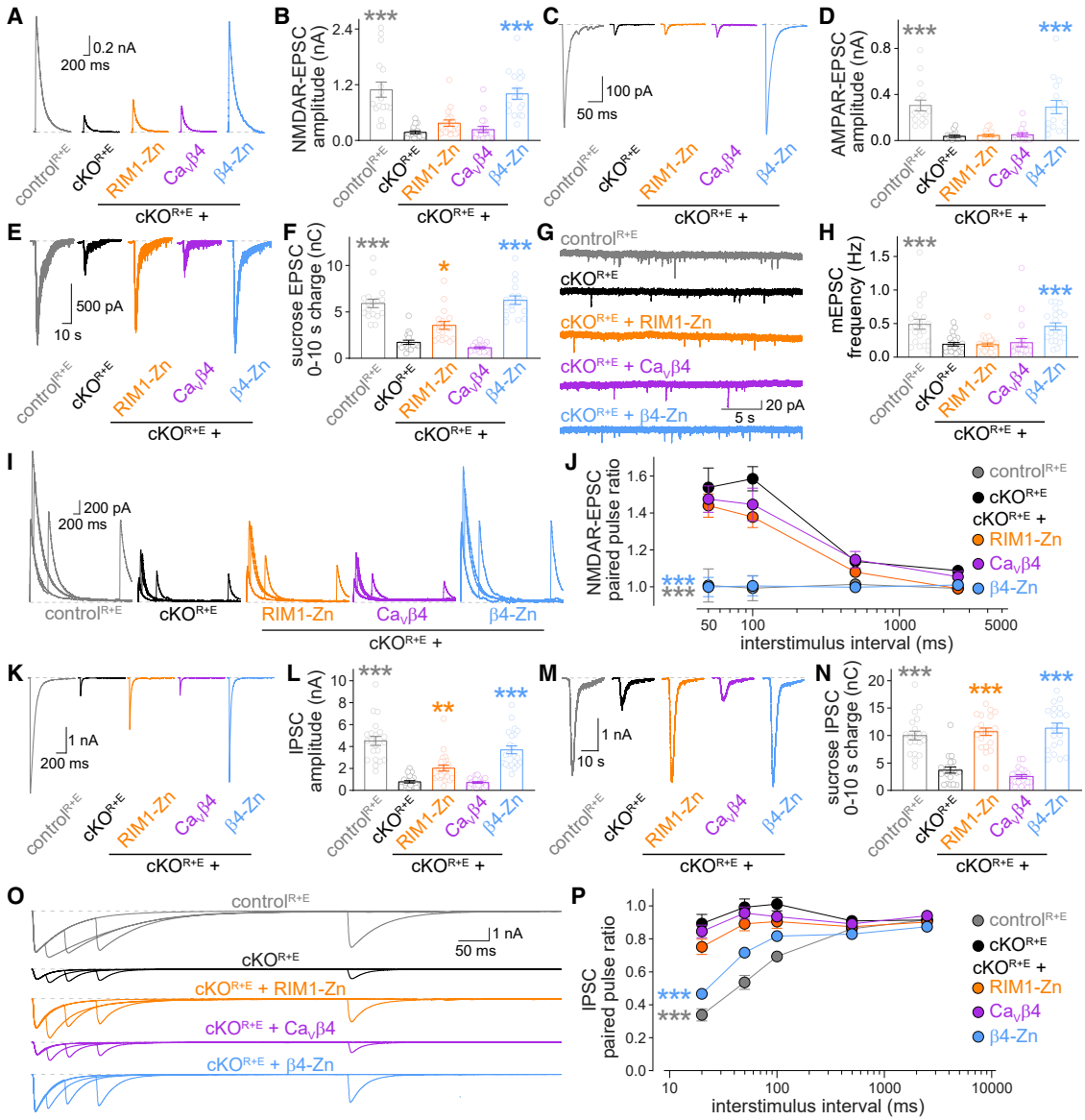

Figure 6. β4-Zn reconstitutes vesicle release in neurons with disrupted active zones

(A–D) Sample traces (A and C) and quantification (B and D) of EPSCs (A and B: NMDAR, C and D: AMPAR) evoked by focal electrical stimulation, (B): control^{R+E} 17 cells/3 cultures, cKO^{R+E} 17/3, cKO^{R+E} + RIM1-Zn 18/3, cKO^{R+E} + $Ca_V\beta4$ 18/3, and cKO^{R+E} + β4-Zn 17/3; (D): 16/3 each.

(E and F) Sample traces (E) and quantification (F) of EPSCs triggered by hypertonic sucrose, 17/3 each.

(G and H) Sample traces (G) and quantification of mEPSC frequencies (H), control^{R+E} 21/3, cKO^{R+E} 23/3, cKO^{R+E} + RIM1-Zn 23/3, cKO^{R+E} + $Ca_V\beta4$ 22/3, and cKO^{R+E} + β4-Zn 21/3.

(I and J) Sample traces (I) and quantification (J) of EPSC paired pulse ratios, control^{R+E} 16/3, cKO^{R+E} 16/3, cKO^{R+E} + RIM1-Zn 17/3, cKO^{R+E} + $Ca_V\beta4$ 16/3, and cKO^{R+E} + β4-Zn 17/3.

(K–P) As (A–F, I, and J), but for electrically evoked IPSCs (K and L), sucrose-evoked IPSCs (M and N), and IPSC paired pulse ratios (O and P), (L): control^{R+E} 21/4, cKO^{R+E} 21/4, cKO^{R+E} + RIM1-Zn 24/4, cKO^{R+E} + $Ca_V\beta4$ 22/4, and cKO^{R+E} + β4-Zn 22/4; (N): 20/3 each; (P): control^{R+E} 20/4, cKO^{R+E} 19/4, cKO^{R+E} + RIM1-Zn 20/4, cKO^{R+E} + $Ca_V\beta4$ 19/4, and cKO^{R+E} + β4-Zn 20/4.

Data are mean ± SEM; *p < 0.05, **p < 0.01, ***p < 0.001 compared with cKO^{R+E} as determined by Kruskal-Wallis tests followed by Dunn's multiple comparisons post hoc tests (B, D, F, H, L, and N) or by two-way ANOVA followed by Dunnett's tests (J and P). For assessment of mEPSC amplitudes and kinetics, and Ca^{2+}-, EGTA-, and sucrose concentration-dependence of release, see Figure S6.

channels, we introduced K144E + K146E point mutations into the RIM zinc finger domain of β4-Zn (generating β4-Zn$^{K144/146E}$). It was previously established that this mutation abolishes binding of the RIM zinc finger to Munc13 (Deng et al., 2011; Dulubova et al., 2005). β4-Zn$^{K144/146E}$ was efficiently expressed and localized to the active zone area of the plasma membrane (Figures 7A–7C

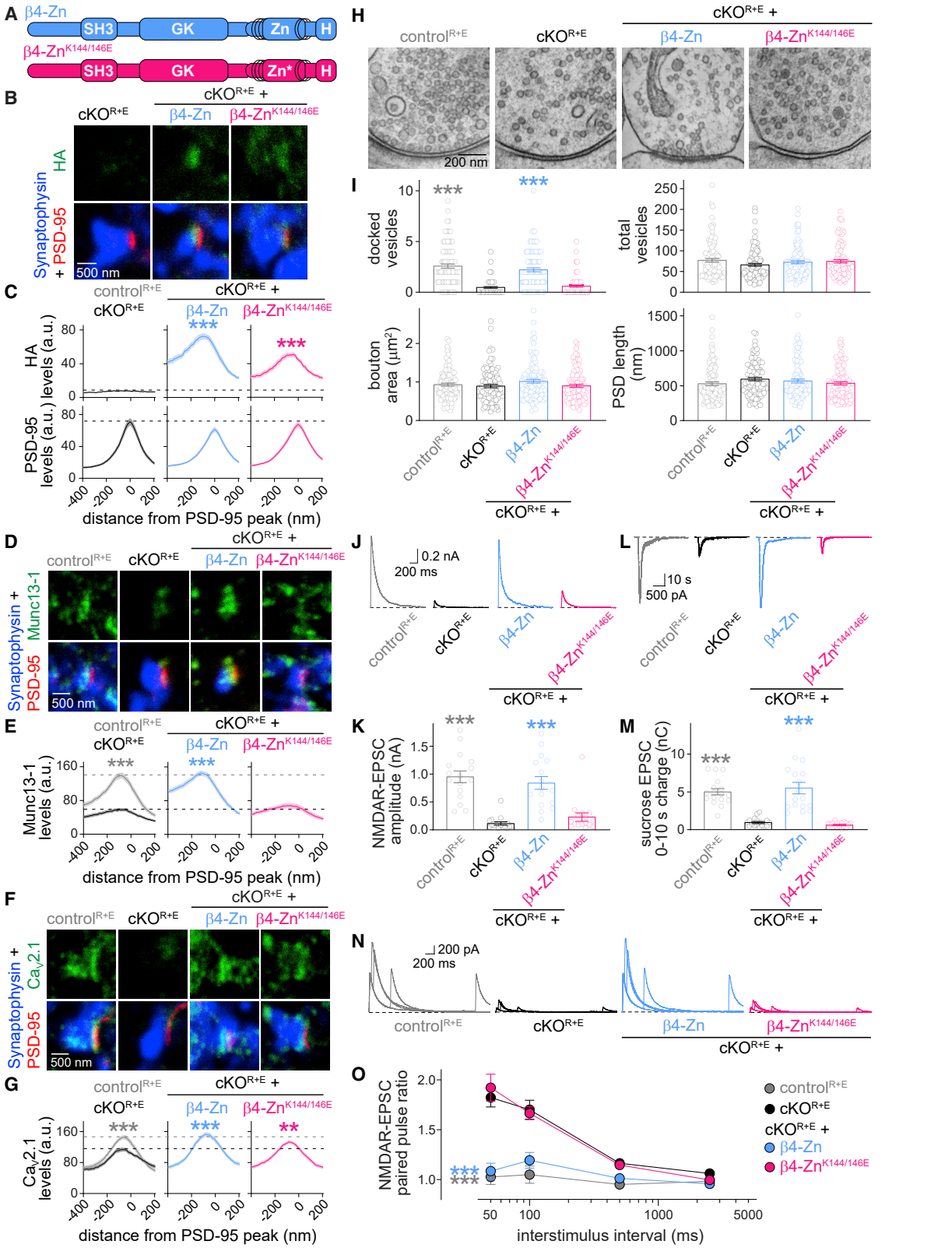

(legend on next page)

and S7A). Abolishing Munc13 binding in β4-Zn$^{K144/146E}$ resulted in a loss of Munc13-1 recruitment to the target membrane (Figures 7D and 7E). While β4-Zn$^{K144/146E}$ was still sufficient to mediate some enhancement of $Ca_V2.1$ levels, it appeared less efficient than β4-Zn (Figures 7F and 7G), quantitatively matching with the somewhat lower β4-Zn$^{K144/146E}$ active zone levels (Figures 7B and 7C). Disrupting binding of β4-Zn to Munc13 completely abolished rescue of vesicle docking (Figures 7H and 7I) and of synaptic strength, RRP, and p at both excitatory (Figures 7J–7O) and inhibitory (Figures S7B–S7G) synapses. These data strongly support the model that β4-Zn restores exocytosis via recruitment of Munc13 and vesicle docking.

Directing Munc13 and vesicle tethering away from the active zone

Some of the mechanisms of β4-Zn might rely on the remaining active zone scaffolds, for example, Liprin-α. To test whether β4-Zn can recruit Munc13-1 to Ca_V2 channels independent of these remaining scaffolds, we assessed localization of β4-Zn-mVenus and Munc13-1-tdTomato in transfected HEK293T cells with or without Cerulean-$Ca_V2.1$ (Figure 8A, all transfections also contained untagged α2δ1 proteins). When $Ca_V2.1$ was present, β4-Zn and Munc13-1 were targeted to the cell periphery similar to $Ca_V2.1$ channels (Figures 8B–8E). Hence, the docking complex of RIM zinc fingers and Munc13 can be attached to Ca^{2+} channels without co-expression of other active zone proteins. We next tested whether this complex is sufficient to tether vesicles on membranes other than the presynaptic plasma membrane. We mistargeted Cerulean-tagged RIM1-Zn to mitochondria by fusing it to the transmembrane region of the outer leaflet mitochondrial protein Tom20 (Kanaji et al., 2000; Nyitrai et al., 2020) to generate mito-Cerulean-Zn (mitoC-Zn) and used mito-Cerulean (mitoC) as a control (Figure 8F). Lentiviral transduction of cKO^{R+E} neurons resulted in robust mitoC-Zn and mitoC expression and the proteins localized to mitochondria (Figures S8A and S8B). MitoC-Zn enhanced Munc13-1 levels measured in mitochondrial ROIs (Figures 8G and 8H), suggesting that the mitochondrial-targeted RIM zinc finger is sufficient to recruit Munc13-1 to mitochondria. Moreover, mitoC-Zn increased the tethering of vesicles to the surface of axonal mitochondria (Figures 8I–8K) as assessed in electron microscopy. Synaptic ultrastructure and vesicle docking were unaltered by mitoC or mitoC-Zn compared with cKO^{R+E} (Figures S8C and S8D). Hence, targeting of RIM1-Zn to mitochondria is sufficient to recruit Munc13-1 and to tether some vesicles to these mitochondria.

DISCUSSION

The active zone is a molecular machine that is important for synaptic signaling (Emperador-Melero and Kaeser, 2020; Südhof, 2012), and many brain disorders are associated with mutations in active zone proteins or defective active zone function (Benarroch, 2013; Bucan et al., 2009; Johnson et al., 2003; Krumm et al., 2015; O'Roak et al., 2012; Thevenon et al., 2013; Verhage and Sørensen, 2020). However, understanding its mechanisms and restoring its functions have remained challenging because of the molecular complexity of the active zone. Here, we develop a reconstitution approach within a synapse after we remove active zone protein machinery. We find that synaptic strength and temporal precision of vesicle release can be restored by positioning the RIM zinc finger, a small protein domain that recruits the priming protein Munc13, to presynaptic Ca^{2+} channels. Our work further reveals that Munc13 is positioned with RIM zinc fingers even when the zinc finger is mistargeted to other cellular compartments: if RIM zinc fingers are localized to undocked vesicles, Munc13 is co-recruited and enhances fusogenicity of these vesicles; if it is targeted to Ca_V2 channels expressed at the plasma membrane of HEK293T cells, Munc13 is tethered to these channels; if it is localized on neuronal mitochondria, these mitochondria can recruit Munc13 and some vesicles to their surface. Ultimately, our results establish that most active zone scaffolds can be bypassed with an 80-kDa β4-Zn protein that docks fusion-competent vesicles close to presynaptic Ca^{2+} channels, and these vesicles can be rapidly released in response to action potentials (Figures 8L–8N).

Flexible order of priming and docking as a vesicle is prepared for release

Our results mechanistically define the two fundamental presynaptic processes: vesicle fusogenicity can be generated by activated Munc13 independent of its active zone positioning, and Ca^{2+} secretion coupling is mediated by docking of Munc13-associated synaptic vesicles next to Ca^{2+} channels. Past studies have discovered that these processes rely on many proteins, and each active zone protein has contributed to each active zone function (Emperador-Melero et al., 2021; Acuna et al., 2015; Aravamudan et al., 1999; Augustin et al., 1999; Brockmann

Figure 7. Binding of β4-Zn to Munc13 mediates Munc13 recruitment, vesicle docking, and release

(A) Schematic of rescue proteins.

(B and C) Sample STED images (C) and quantification (D) of side-view synapses stained for HA (STED), PSD-95 (STED), and synaptophysin (confocal), dotted lines mark cKO^{R+E} levels for comparison, 60 synapses/3 cultures each.

(D–G) Same as (B and C), but for Munc13-1 (D and E) and $Ca_V2.1$ (F and G), 60/3 each. PSD-95 levels were similar across conditions, but are not shown for simplicity, dotted lines mark control^{R+E} (gray) and cKO^{R+E} (black) levels for comparison.

(H and I) Sample electron microscopic images (H) and analyses (I) of synapses of high-pressure-frozen neurons, control^{R+E} 100 synapses/2 cultures, cKO^{R+E} 99/2, cKO^{R+E} + β4-Zn 99/2, and cKO^{R+E} + β4-Zn$^{K144/146E}$ 99/2.

(J and K) Sample traces (J) and quantification (K) of EPSCs evoked by focal electrical stimulation, 16 cells/4 cultures each.

(L and M) Sample traces (L) and quantification (M) of EPSCs triggered by hypertonic sucrose, 17/3 each.

(N and O) Sample traces (N) and quantification (O) of EPSC paired pulse ratios, 16/4 each.

Data are mean ± SEM; $^{**}p < 0.01$, $^{***}p < 0.001$ compared with cKO^{R+E} as determined by two-way ANOVA followed by Dunnett's tests (C, E, G, and O), Brown-Forsythe ANOVA followed by Games-Howell's multiple comparisons post hoc test (I, docked vesicles), or by Kruskal-Wallis tests followed by Dunn's multiple comparisons post hoc tests (K and M). For assessment of rescue protein expression, and for recordings of IPSCs with β4-Zn$^{K144/146E}$ expression, see Figure S7.

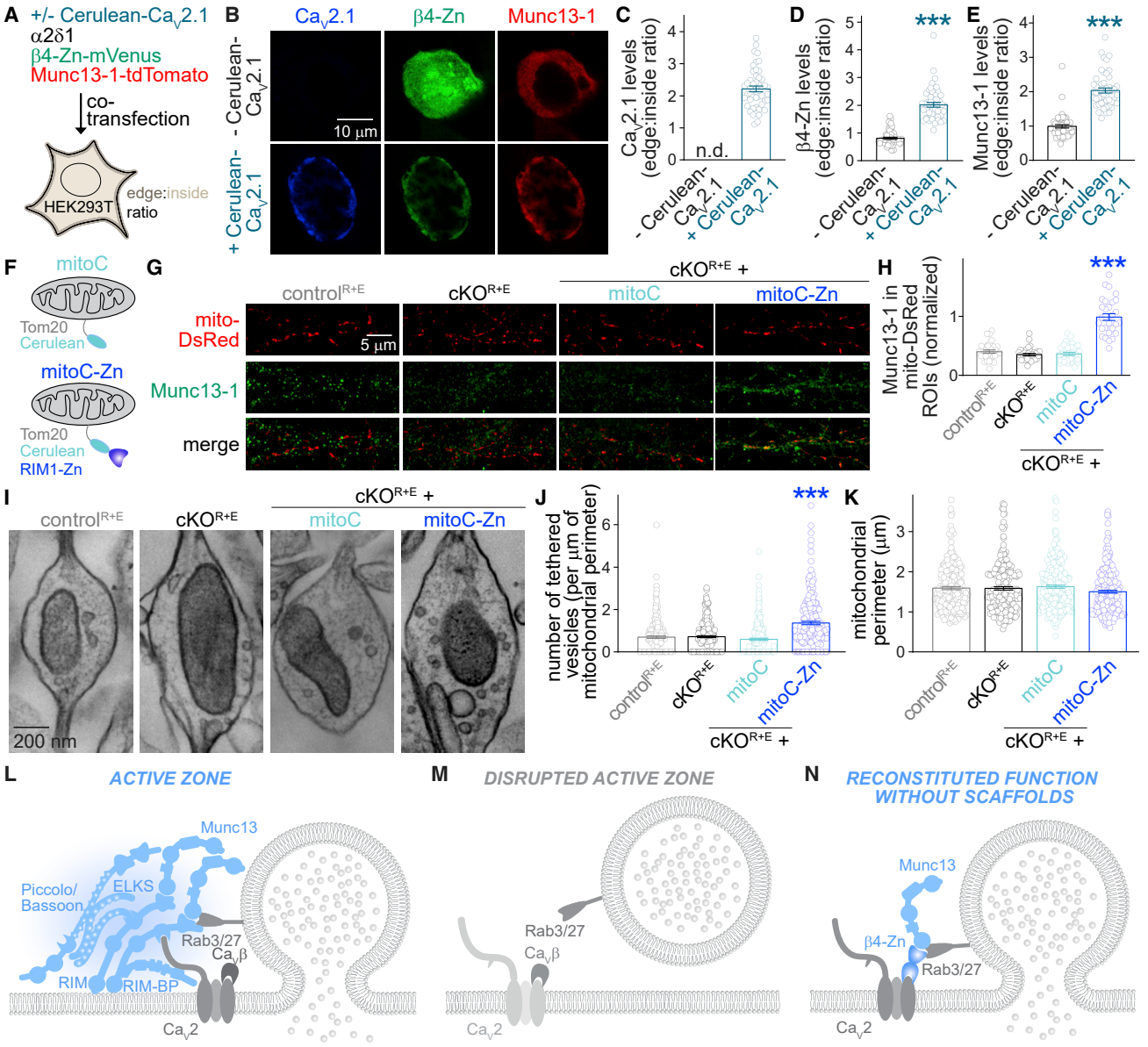

Figure 8. Redirecting the docking complex to other membranes and working model

(A) Schematic of experiments in transfected HEK293T cells.

(B–E) Sample confocal images (B) and quantification of edge:inside ratio for $Ca_V2.1$ (C), β4-Zn (D), and Munc13-1 (E), 48 cells/3 transfections each.

(F) Schematic of targeting of RIM1-Zn to mitochondria in neurons.

(G, H) Representative confocal images (G) and quantification of Munc13-1 levels (H) in mitochondrial ROIs in control^{R+E} and cKO^{R+E} neurons and in cKO^{R+E} neurons transduced with lentiviruses expressing mitoC or mitoC-Zn (and mito-DsRed in all conditions), 30 images/3 cultures each.

(I–K) Sample electron microscopic images (I) and quantification (J, K) of vesicles tethered to the surface of axonal mitochondria, control^{R+E} 221 mitochondria/2 cultures, cKO^{R+E} 218/2, cKO^{R+E} + mitoC 218/2, and cKO^{R+E} + mitoC-Zn 215/2.

(L–N) Working model of the presynaptic active zone (L, adapted from previous models [Biederer et al., 2017; de Jong et al., 2018; Kaeser et al., 2011]). RIM+ELKS knockout leads to loss of many active zone scaffolds and to impaired vesicle docking, priming, and release (M). Reconstitution of synaptic function is mediated by a β4-Zn fusion protein that docks primed vesicles close to Ca^{2+} channels in the absence of most active zone scaffolds (N).

Data are mean ± SEM; ***p < 0.001 as determined by Welch's t test (D and E, compared with −Cerulean-$Ca_V2.1$) or by Brown-Forsythe ANOVA followed by Dunnett's T3 multiple comparisons post hoc test (H, compared with cKO^{R+E}) and by Brown-Forsythe ANOVA followed by Games-Howell's multiple comparisons post hoc test (J, compared with cKO^{R+E}). For protein expression analyses, assessment of mitoC-Zn localization by confocal microscopy, and additional analyses of electron microscopic images, see Figure S8.

et al., 2019; Davydova et al., 2014; Deng et al., 2011; Dong et al., 2018; ; Grauel et al., 2016; Held et al., 2016; Imig et al., 2014'Kaeser et al., 2011; Kawabe et al., 2017; Kittel et al., 2006; Koushika et al., 2001; Lipstein et al., 2013; Liu et al., 2014, 2011; Matkovic et al., 2013; Richmond et al., 1999; Schoch et al., 2002; Varoqueaux et al., 2002; Wong et al., 2018; Zarebidaki et al., 2020; Zhen and Jin, 1999). These findings reflect that the active zone is a complex protein network with built-in redundancy. Knockout studies may lead to alterations of the entire network and not necessarily reveal highly specific mechanisms of isolated proteins. Hence, it has been difficult to define which proteins and mechanisms drive vesicle priming, docking, and release. Our approach establishes that these functions can be executed even if most of these proteins are removed. Vesicle priming can be mediated by the RIM zinc finger domain, which is sufficient to recruit, stabilize, and activate Munc13. When this mechanism is positioned close to Ca^{2+} channels, release triggering is restored.

Models of neurotransmitter release propose that vesicle docking either precedes vesicle priming or occurs simultaneously with it (Hammarlund et al., 2007; Imig et al., 2014, 2020; Rosenmund and Stevens, 1996; Schikorski and Stevens, 2001; Sudhof, 2004) and that Munc13 mediates both roles through the control of SNARE complex assembly (Basu et al., 2005; Imig et al., 2014; Ma et al., 2013; Siksou et al., 2009; Südhof, 2012). In view of this literature, it is surprising that vesicle priming, or fusogenicity, can be generated in the absence of docking (Figure 4). This challenges the linear docking-priming model that relies on SNARE complex assembly. Our data instead reveal that the generation of fusion-competent vesicles and vesicle docking are molecularly separable processes and that vesicles away from the active zone can be activated for fusion. We propose that the rate-limiting step is not SNARE complex assembly, as this necessitates the coincidence of docking and priming, but instead the availability and activation of Munc13. This is supported by the observation that fusion-competent vesicles can be generated by positioning Munc13 on undocked vesicles (Figures 3 and 4), by the notion that some fusion-competent vesicles remain when Munc13 is displaced from the active zone (Wang et al., 2016), and by the finding that knockout of RIM, which is upstream of Munc13's role in vesicle priming, leads to strong impairments in RRP (Calakos et al., 2004; Deng et al., 2011; Han et al., 2011). While Munc13 mediates both synaptic vesicle docking and priming (Augustin et al., 1999; Imig et al., 2014; Varoqueaux et al., 2002), generating fusion competence and vesicle docking are separable, at least after disrupting active zone structure. We propose that, while many RRP vesicles are docked (Borges-Merjane et al., 2020; Imig et al., 2014, 2020; Schikorski and Stevens, 2001), the presence and activation of Munc13 embody the bottleneck for vesicle priming. Munc13-mediated SNARE complex assembly may not be rate limiting for vesicle release and may occur before or during fusion.

Streamlined active zone assembly bypasses the need for complex scaffolds

Mechanisms and hierarchy of active zone protein recruitment have remained difficult to establish. Our work reveals that the RIM PDZ domain is important for recruitment of RIM to the active zone, as removing it prevents RIM active zone targeting. Furthermore, our data indicate that RIM drives recruitment of presynaptic protein machinery. RIM re-expression restores levels of all other active zone proteins and of Ca^{2+} channels, and more RIM drives the presence of more Munc13, Ca^{2+} channels, and other active zone proteins. Recent work proposed that liquid-liquid phase separation of RIM, RIM-BP, and Ca_V2s mediates active zone assembly (Wu et al., 2019, 2021). Our work is consistent with this model and indicates that phase condensation of RIM and RIM-BP into liquid droplets is not necessary for neurotransmitter release per se, as fusing the RIM zinc finger domain to $Ca_V\beta4$ restores release in the absence of most RIM and RIM-BP sequences necessary for phase condensation. In principle, it is possible that other liquid phases, which may or may not incorporate Ca_V2s, could be at play. In this context, it is interesting that Liprin-$\alpha3$ levels at the active zone increase upon active zone disruption. Liprin-α undergoes phase condensation and participates in the regulation of active zone structure (Emperador-Melero et al., 2021; McDonald et al., 2020). It is possible, and perhaps likely, that two phases compete or are in equilibrium with one another at a synapse and that removing one enhances the other. This is supported by the enhanced presence of Liprin-$\alpha3$ upon disruption of the active zone protein complex between RIM, ELKS, RIM-BP, Ca_V2s, Munc13, and Bassoon (Figure 1). Conversely, at Liprin-$\alpha2/3$ knockout synapses enhanced levels of Ca_V2 proteins are present (Emperador-Melero et al., 2021). RIM may link the two phases together or participate in both, as its active zone recruitment is decreased upon Liprin-α ablation.

The artificial $\beta4$-Zn fusion protein enhances Ca_V2 active zone levels together with restoring vesicle docking and release. Our experiments assess this for $Ca_V2.1$. The sequence and biochemical similarities of $Ca_V2.1$ and $Ca_V2.2$ and their functional redundancy make it likely that our findings apply to both channels (Cao et al., 2004; Held et al., 2020; Hibino et al., 2002; Kaeser et al., 2011), while roles of $Ca_V2.3$ may be distinct (Breustedt et al., 2003; Dietrich et al., 2003; Myoga and Regehr, 2011; Wu et al., 1999). One possibility is that vesicle docking stabilizes the Ca_V2 protein complex at active zones. This model is supported by the observation that abolishing the docking function of $\beta4$-Zn by preventing its binding to Munc13 appears to revert this effect partially. Another possibility is that $\beta4$-Zn enhances the delivery of Ca_V2s to the active zone and that Munc13 binding is required for this function. Ultimately, our data may suggest that a stable release site contains a docked vesicle, that release sites that do not contain docked vesicles are subject to dynamic rearrangements, and that Ca_V2s of unoccupied release sites may be more mobile (Schneider et al., 2015). An alternative model is that Ca_V2s and exocytotic protein machinery such as Munc13 are in different proteins complexes (Rebola et al., 2019). In this model RIM proteins would participate in distinct assemblies: one may define secretory sites and contain at least RIM and Munc13 (Deng et al., 2011; Emperador-Melero et al., 2021; Reddy-Alla et al., 2017; Sakamoto et al., 2018; Tang et al., 2016), and another controls Ca^{2+} channel clustering and contains RIM, RIM-BP, and Ca_V2s (Acuna et al., 2016; Held et al., 2020; Hibino et al., 2002; Kaeser et al., 2011; Kushibiki et al., 2019; Liu et al., 2011; Oh et al., 2021; Wu et al., 2019). In this model, proteins like

RIM or ELKS could bridge the complexes, and our reconstitution would account for both functions (Figure 8L). Future studies should address these models.

In aggregate, our data suggest that the release machinery assembly requirements are remarkably simple: RIM zinc fingers recruit Munc13 to prime vesicles, and if positioned next to Ca_V2 channels, these vesicles can be rapidly and precisely released (Figures 8L–8N). We propose that synaptic strength is mainly determined through reconstituting these key mechanisms and that other proteins mediate regulatory functions. Some secretory systems, for example, those for striatal dopamine release, may make use of these relatively simple, streamlined mechanisms (Banerjee et al., 2021; Liu et al., 2018).

A small protein for rebuilding the function of a complex machine

Neurotransmitter secretion and sensing are often impaired in brain disease, ranging from highly specific associations of gene mutations in active zone proteins to more generalized breakdown of synaptic signaling, and these diseases are often called synaptopathies (Benarroch, 2013; Bucan et al., 2009; Johnson et al., 2003; Krumm et al., 2015; O'Roak et al., 2012; Thevenon et al., 2013; Verhage and Sørensen, 2020). Advances in adeno-associated virus (AAV)-based gene therapy strategies have spurred new hope for developing treatments for brain disorders (Hudry and Vandenberghe, 2019; Sun and Roy, 2021). However, a key limitation is that synaptic and secretory genes often exceed the packaging size of AAVs (Wu et al., 2010). A recent way to work past this limitation is the use of dual or triple AAVs that contain fragments and that are then spliced to generate whole proteins, for example, for restoration of hearing (Akil et al., 2019; Al-Moyed et al., 2019). Another possibility is to find smaller proteins to restore function. Our reconstitution approach identifies a single 80-kDa protein, the $Ca_V\beta4$-RIM zinc finger fusion, which is well within packaging limits of gene therapy viruses (Hudry and Vandenberghe, 2019; Wu et al., 2010). This relatively small protein can increase synaptic efficacy and is sufficient to mediate temporal precision of release after disrupting active zone architecture. Our approach serves as proof-of-concept for reconstructing functions of a complex molecular machine with relatively simple "pieces" by targeting these key elements to the right subcellular compartment.

STAR★METHODS

Detailed methods are provided in the online version of this paper and include the following:

- KEY RESOURCES TABLE
- RESOURCE AVAILABILITY
  - Lead contact
  - Materials availability
  - Data and code availability
- EXPERIMENTAL MODEL AND SUBJECT DETAILS
  - Animals
  - Primary cultures
  - Cell lines
  - Lentiviruses
  - Rescue and other constructs
  - STED imaging
  - Confocal imaging of cultured neurons
  - Confocal imaging in transfected HEK293T cells
  - Electrophysiology
  - High-pressure freezing and electron microscopy
  - Western blotting
- QUANTIFICATION AND STATISTICAL ANALYSIS

SUPPLEMENTAL INFORMATION

Supplemental information can be found online at https://doi.org/10.1016/j.neuron.2022.01.026.

ACKNOWLEDGMENTS

We thank J. Wang and C. Qiao for technical support, E. Raviola, W. Regehr, R. Held, and H. Nyitrai for insightful discussions and help with setting up experimental approaches, all members of the Kaeser laboratory for feedback, M. Verhage and J. Broeke for a MATLAB macro to analyze electron microscopic images, A.M.J.M. van den Maagdenberg for $Ca_V2.1^{floxed}$ mice, and T. Schneider for $Ca_V2.3^{floxed}$ mice. This work was supported by grants from the NIH (R01MH113349 and R01NS083898 to P.S.K.), the Armenise Harvard Foundation (to P.S.K.), and an NSF graduate research fellowship (DGE1144152 to S.S.H.W.). We acknowledge the Neurobiology Imaging Facility (supported by a P30 Core Center grant P30NS072030), and the Electron Microscopy Facility at Harvard Medical School.

AUTHOR CONTRIBUTIONS

Conceptualization, C.T., S.S.H.W., and P.S.K.; methodology, C.T., S.S.H.W., and G.d.N.; formal analysis, C.T., S.S.H.W., G.d.N., and P.S.K.; investigation, C.T., S.S.H.W., and G.d.N.; resources, C.T. and S.S.H.W.; writing – original draft, C.T. and P.S.K.; writing – review & editing, C.T., G.d.N., and P.S.K.; supervision, P.S.K.; funding acquisition, P.S.K.

DECLARATION OF INTERESTS

The authors declare no competing interests. S.S.H.W. is currently an employee of RA Capital Management, LP.

Received: February 24, 2021
Revised: December 21, 2021
Accepted: January 24, 2022
Published: February 16, 2022

REFERENCES

Acuna, C., Liu, X., Gonzalez, A., and Südhof, T.C. (2015). RIM-BPs mediate tight coupling of action potentials to Ca(2+)-triggered neurotransmitter release. Neuron *87*, 1234–1247.

Acuna, C., Liu, X., and Südhof, T.C. (2016). How to make an active zone: unexpected universal functional redundancy between RIMs and RIM-BPs. Neuron *91*, 792–807.

Akil, O., Dyka, F., Calvet, C., Emptoz, A., Lahlou, G., Nouaille, S., Boutet de Monvel, J., Hardelin, J.-P., Hauswirth, W.W., Avan, P., et al. (2019). Dual AAV-mediated gene therapy restores hearing in a DFNB9 mouse model. Proc. Natl. Acad. Sci. USA *116*, 4496–4501.

Al-Moyed, H., Cepeda, A.P., Jung, S., Moser, T., Kügler, S., and Reisinger, E. (2019). A dual-AAV approach restores fast exocytosis and partially rescues auditory function in deaf otoferlin knock-out mice. EMBO Mol. Med. *11*, 4496–4501.

Aravamudan, B., Fergestad, T., Davis, W.S., Rodesch, C.K., and Broadie, K. (1999). Drosophila UNC-13 is essential for synaptic transmission. Nat. Neurosci. *2*, 965–971.

Augustin, I., Rosenmund, C., Südhof, T.C., and Brose, N. (1999). Munc13-1 is essential for fusion competence of glutamatergic synaptic vesicles. Nature *400*, 457–461.

Banerjee, A., Imig, C., Balakrishnan, K., Kershberg, L., Lipstein, N., Uronen, R.-L., Wang, J., Cai, X., Benseler, F., Rhee, J.S., et al. (2021). Molecular and functional architecture of striatal dopamine release sites. Neuron *110*, 248–265, e9.

Basu, J., Shen, N., Dulubova, I., Lu, J., Guan, R., Guryev, O., Grishin, N.V., Rosenmund, C., and Rizo, J. (2005). A minimal domain responsible for Munc13 activity. Nat. Struct. Mol. Biol. *12*, 1017–1018.

Benarroch, E.E. (2013). Synaptic vesicle exocytosis: molecular mechanisms and clinical implications. Neurology *80*, 1981–1988.

Betz, A., Thakur, P., Junge, H.J., Ashery, U., Rhee, J.S., Scheuss, V., Rosenmund, C., Rettig, J., and Brose, N. (2001). Functional interaction of the active zone proteins Munc13-1 and RIM1 in synaptic vesicle priming. Neuron *30*, 183–196.

Biederer, T., Kaeser, P.S., and Blanpied, T.A. (2017). Transcellular nanoalignment of synaptic function. Neuron *96*, 680–696.

Borges-Merjane, C., Kim, O., and Jonas, P. (2020). Functional electron microscopy, "flash and freeze," of identified cortical synapses in acute brain slices. Neuron *105*, 992–1006.e6.

Breustedt, J., Vogt, K.E., Miller, R.J., Nicoll, R.A., and Schmitz, D. (2003). Alpha1E-containing Ca2+ channels are involved in synaptic plasticity. Proc. Natl. Acad. Sci. USA *100*, 12450–12455.

Brockmann, M.M., Maglione, M., Willmes, C.G., Stumpf, A., Bouazza, B.A., Velasquez, L.M., Grauel, M.K., Beed, P., Lehmann, M., Gimber, N., et al. (2019). RIM-BP2 primes synaptic vesicles via recruitment of Munc13-1 at hippocampal mossy fiber synapses. Elife *8*, e43243.

Bucan, M., Abrahams, B.S., Wang, K., Glessner, J.T., Herman, E.I., Sonnenblick, L.I., Alvarez Retuerto, A.I., Imielinski, M., Hadley, D., Bradfield, J.P., et al. (2009). Genome-wide analyses of exonic copy number variants in a family-based study point to novel autism susceptibility genes. PLoS Genet *5*, e1000536.

Calakos, N., Schoch, S., Sudhof, T.C., Malenka, R.C., Südhof, T.C., Malenka, R.C., Sudhof, T.C., and Malenka, R.C. (2004). Multiple roles for the active zone protein RIM1alpha in late stages of neurotransmitter release. Neuron *42*, 889–896.

Camacho, M., Basu, J., Trimbuch, T., Chang, S., Pulido-Lozano, C., Chang, S.-S., Duluvova, I., Abo-Rady, M., Rizo, J., and Rosenmund, C. (2017). Heterodimerization of Munc13 C2A domain with RIM regulates synaptic vesicle docking and priming. Nat. Commun. *8*, 15293.

Cao, Y.Q., Piedras-Rentería, E.S., Smith, G.B., Chen, G., Harata, N.C., and Tsien, R.W. (2004). Presynaptic Ca2+ channels compete for channel type-preferring slots in altered neurotransmission arising from Ca2+ channelopathy. Neuron *43*, 387–400.

Davydova, D., Marini, C., King, C., Klueva, J., Bischof, F., Romorini, S., Montenegro-Venegas, C., Heine, M., Schneider, R., Schröder, M.S., et al. (2014). Bassoon specifically controls presynaptic P/Q-type Ca(2+) channels via RIM-binding protein. Neuron *82*, 181–194.

de Jong, A.P.H., Roggero, C.M., Ho, M.-R., Wong, M.Y., Brautigam, C.A., Rizo, J., and Kaeser, P.S. (2018). RIM C2B domains target presynaptic active zone functions to PIP2-containing membranes. Neuron *98*, 335–349.e7.

Deng, L., Kaeser, P.S., Xu, W., and Südhof, T.C. (2011). RIM proteins activate vesicle priming by reversing autoinhibitory homodimerization of Munc13. Neuron *69*, 317–331.

Dietrich, D., Kirschstein, T., Kukley, M., Pereverzev, A., von der Brelie, C., Schneider, T., and Beck, H. (2003). Functional specialization of presynaptic Cav2.3 Ca2+ channels. Neuron *39*, 483–496.

Dolphin, A.C. (2012). Calcium channel auxiliary α2δ and β subunits: trafficking and one step beyond. Nat. Rev. Neurosci. *13*, 542–555.

Dong, W., Radulovic, T., Goral, R.O., Thomas, C., Suarez Montesinos, M., Guerrero-Given, D., Hagiwara, A., Putzke, T., Hida, Y., Abe, M., et al. (2018). CAST/ELKS proteins control voltage-gated Ca2+ channel density and synaptic release probability at a mammalian central synapse. Cell Rep *24*, 284–293.e6.

Dulubova, I., Lou, X., Lu, J., Huryeva, I., Alam, A., Schneggenburger, R., Südhof, T.C., and Rizo, J. (2005). A Munc13/RIM/Rab3 tripartite complex: from priming to plasticity? EMBO J *24*, 2839–2850.

Emperador-Melero, J., and Kaeser, P.S. (2020). Assembly of the presynaptic active zone. Curr. Opin. Neurobiol. *63*, 95–103.

Emperador-Melero, J., Wong, M.Y., Wang, S.S.H., de Nola, G., Nyitrai, H., Kirchhausen, T., and Kaeser, P.S. (2021). PKC-phosphorylation of liprin-α3 triggers phase separation and controls presynaptic active zone structure. Nat. Commun. *12*, 3057.

Fukuda, M. (2003). Distinct Rab binding specificity of Rim1, Rim2, rabphilin, and Noc2. Identification of a critical determinant of Rab3A/Rab27A recognition by Rim2. J. Biol. Chem. *278*, 15373–15380.

Grauel, M.K., Maglione, M., Reddy-Alla, S., Willmes, C.G., Brockmann, M.M., Trimbuch, T., Rosenmund, T., Pangalos, M., Vardar, G., Stumpf, A., et al. (2016). RIM-binding protein 2 regulates release probability by fine-tuning calcium channel localization at murine hippocampal synapses. Proc. Natl. Acad. Sci. USA *113*, 11615–11620.

Guzman, G.A., Guzman, R.E., Jordan, N., and Hidalgo, P. (2019). A tripartite interaction among the calcium channel α1- and β-subunits and F-actin increases the readily releasable pool of vesicles and its recovery after depletion. Front. Cell. Neurosci. *13*, 125.

Hammarlund, M., Palfreyman, M.T., Watanabe, S., Olsen, S., and Jorgensen, E.M. (2007). Open syntaxin docks synaptic vesicles. PLoS Biol *5*, e198.

Han, W., Rhee, J.-S., Maximov, A., Lao, Y., Mashimo, T., Rosenmund, C., and Südhof, T.C. (2004). N-glycosylation is essential for vesicular targeting of synaptotagmin 1. Neuron *41*, 85–99.

Han, Y., Kaeser, P.S., Südhof, T.C., and Schneggenburger, R. (2011). RIM determines Ca2+ channel density and vesicle docking at the presynaptic active zone. Neuron *69*, 304–316.

He, E., Wierda, K., van Westen, R., Broeke, J.H., Toonen, R.F., Cornelisse, L.N., and Verhage, M. (2017). Munc13-1 and Munc18-1 together prevent NSF-dependent de-priming of synaptic vesicles. Nat. Commun. *8*, 15915.

Held, R.G., and Kaeser, P.S. (2018). ELKS active zone proteins as multitasking scaffolds for secretion. Open Biol *8*, 29491150.

Held, R.G., Liu, C., and Kaeser, P.S. (2016). ELKS controls the pool of readily releasable vesicles at excitatory synapses through its N-terminal coiled-coil domains. Elife *5*, e14862.

Held, R.G., Liu, C., Ma, K., Ramsey, A.M., Tarr, T.B., De Nola, G., Wang, S.S.H., Wang, J., van den Maagdenberg, A.M.J.M., Schneider, T., et al. (2020). Synapse and active zone assembly in the absence of presynaptic Ca2+ channels and Ca2+ entry. Neuron *107*, 667–683.e9.

Hibino, H., Pironkova, R., Onwumere, O., Vologodskaia, M., Hudspeth, A.J., and Lesage, F. (2002). RIM binding proteins (RBPs) couple Rab3-interacting molecules (RIMs) to voltage-gated Ca(2+) channels. Neuron *34*, 411–423.

Hu, C., Ahmed, M., Melia, T.J., Söllner, T.H., Mayer, T., Rothman, J.E., Sollner, T.H., Mayer, T., and Rothman, J.E. (2003). Fusion of cells by flipped SNAREs. Science *300*, 1745–1749.

Hudry, E., and Vandenberghe, L.H. (2019). Therapeutic AAV gene transfer to the nervous system: a clinical reality. Neuron *101*, 839–862.

Imig, C., López-Murcia, F.J., Maus, L., García-Plaza, I.H., Mortensen, L.S., Schwark, M., Schwarze, V., Angibaud, J., Nägerl, U.V., Taschenberger, H., et al. (2020). Ultrastructural imaging of activity-dependent synaptic membrane-trafficking events in cultured brain slices. Neuron *108*, 843–860, e8.

Imig, C., Min, S.W., Krinner, S., Arancillo, M., Rosenmund, C., Südhof, T.C., Rhee, J.S., Brose, N., and Cooper, B.H. (2014). The morphological and molecular nature of synaptic vesicle priming at presynaptic active zones. Neuron *84*, 416–431.

Johnson, S., Halford, S., Morris, A.G., Patel, R.J., Wilkie, S.E., Hardcastle, A.J., Moore, A.T., Zhang, K., and Hunt, D.M. (2003). Genomic organisation and alternative splicing of human RIM1, a gene implicated in autosomal dominant cone-rod dystrophy (CORD7). Genomics *81*, 304–314.

Kaeser, P.S., Deng, L., Chávez, A.E., Liu, X., Castillo, P.E., and Südhof, T.C. (2009). ELKS2alpha/CAST deletion selectively increases neurotransmitter release at inhibitory synapses. Neuron *64*, 227–239.

Kaeser, P.S., Deng, L., Wang, Y., Dulubova, I., Liu, X., Rizo, J., and Südhof, T.C. (2011). RIM proteins tether Ca2+ channels to presynaptic active zones via a direct PDZ-domain interaction. Cell *144*, 282–295.

Kaeser, P.S., Kwon, H.B., Chiu, C.Q., Deng, L., Castillo, P.E., and Südhof, T.C. (2008). RIM1alpha and RIM1beta are synthesized from distinct promoters of the RIM1 gene to mediate differential but overlapping synaptic functions. J. Neurosci. *28*, 13435–13447.

Kaeser, P.S., and Regehr, W.G. (2017). The readily releasable pool of synaptic vesicles. Curr. Opin. Neurobiol. *43*, 63–70.

Kanaji, S., Iwahashi, J., Kida, Y., Sakaguchi, M., and Mihara, K. (2000). Characterization of the signal that directs Tom20 to the mitochondrial outer membrane. J. Cell Biol. *151*, 277–288.

Kawabe, H., Mitkovski, M., Kaeser, P.S., Hirrlinger, J., Opazo, F., Nestvogel, D., Kalla, S., Fejtova, A., Verrier, S.E., Bungers, S.R., et al. (2017). ELKS1 localizes the synaptic vesicle priming protein bMunc13-2 to a specific subset of active zones. J. Cell Biol. *216*, 1143–1161.

Kittel, R.J., Wichmann, C., Rasse, T.M., Fouquet, W., Schmidt, M., Schmid, A., Wagh, D.A., Pawlu, C., Kellner, R.R., Willig, K.I., et al. (2006). Bruchpilot promotes active zone assembly, Ca2+ channel clustering, and vesicle release. Science *312*, 1051–1054.

Koushika, S.P., Richmond, J.E., Hadwiger, G., Weimer, R.M., Jorgensen, E.M., and Nonet, M.L. (2001). A post-docking role for active zone protein Rim. Nat. Neurosci. *4*, 997–1005.

Krumm, N., Turner, T.N., Baker, C., Vives, L., Mohajeri, K., Witherspoon, K., Raja, A., Coe, B.P., Stessman, H.A., He, Z.-X., et al. (2015). Excess of rare, inherited truncating mutations in autism. Nat. Genet. *47*, 582–588.

Kushibiki, Y., Suzuki, T., Jin, Y., and Taru, H. (2019). RIMB-1/RIM-binding protein and UNC-10/RIM redundantly regulate presynaptic localization of the voltage-gated calcium channel in *Caenorhabditis elegans*. J. Neurosci. *39*, 8617–8631.

Lin, Y., McDonough, S.I., and Lipscombe, D. (2004). Alternative splicing in the voltage-sensing region of N-type CaV2.2 channels modulates channel kinetics. J. Neurophysiol. *92*, 2820–2830.

Lipstein, N., Sakaba, T., Cooper, B.H., Lin, K.-H., Strenzke, N., Ashery, U., Rhee, J.-S., Taschenberger, H., Neher, E., and Brose, N. (2013). Dynamic control of synaptic vesicle replenishment and short-term plasticity by Ca(2+)-calmodulin-Munc13-1 signaling. Neuron *79*, 82–96.

Liu, C., Bickford, L.S., Held, R.G., Nyitrai, H., Südhof, T.C., and Kaeser, P.S. (2014). The active zone protein family ELKS supports Ca2+ influx at nerve terminals of inhibitory hippocampal neurons. J. Neurosci. *34*, 12289–12303.

Liu, C., Kershberg, L., Wang, J., Schneeberger, S., and Kaeser, P.S. (2018). Dopamine secretion is mediated by sparse active zone-like release sites. Cell *172*, 706–718.e15.

Liu, K.S.Y., Siebert, M., Mertel, S., Knoche, E., Wegener, S., Wichmann, C., Matkovic, T., Muhammad, K., Depner, H., Mettke, C., et al. (2011). RIM-binding protein, a central part of the active zone, is essential for neurotransmitter release. Science *334*, 1565–1569.

Ma, C., Su, L., Seven, A.B., Xu, Y., and Rizo, J. (2013). Reconstitution of the vital functions of Munc18 and Munc13 in neurotransmitter release. Science *339*, 421–425.

Matkovic, T., Siebert, M., Knoche, E., Depner, H., Mertel, S., Owald, D., Schmidt, M., Thomas, U., Sickmann, A., Kamin, D., et al. (2013). The Bruchpilot cytomatrix determines the size of the readily releasable pool of synaptic vesicles. J. Cell Biol. *202*, 667–683.

McDonald, N.A., Fetter, R.D., and Shen, K. (2020). Assembly of synaptic active zones requires phase separation of scaffold molecules. Nature *588*, 454–458.

Myoga, M.H., and Regehr, W.G. (2011). Calcium microdomains near R-type calcium channels control the induction of presynaptic long-term potentiation at parallel fiber to Purkinje cell synapses. J. Neurosci. *31*, 5235–5243.

Nyitrai, H., Wang, S.S.H., and Kaeser, P.S. (2020). ELKS1 captures Rab6-marked vesicular cargo in presynaptic nerve terminals. Cell Rep *31*, 107712.

O'Roak, B.J., Vives, L., Girirajan, S., Karakoc, E., Krumm, N., Coe, B.P., Levy, R., Ko, A., Lee, C., Smith, J.D., et al. (2012). Sporadic autism exomes reveal a highly interconnected protein network of *de novo* mutations. Nature *485*, 246–250.

Oh, K.H., Krout, M.D., Richmond, J.E., and Kim, H. (2021). UNC-2 CaV2 channel localization at presynaptic active zones depends on UNC-10/RIM and SYD-2/liprin-α in *Caenorhabditis elegans*. J. Neurosci. *41*, 4782–4794.

Page, K.M., Rothwell, S.W., and Dolphin, A.C. (2016). The CaVβ subunit protects the I-II loop of the voltage-gated calcium channel CaV2.2 from proteasomal degradation but not oligoubiquitination. J. Biol. Chem. *291*, 20402–20416.

Parthier, D., Kuner, T., and Körber, C. (2018). The presynaptic scaffolding protein Piccolo organizes the readily releasable pool at the calyx of held. J. Physiol. *596*, 1485–1499.

Pereverzev, A., Mikhna, M., Vajna, R., Gissel, C., Henry, M., Weiergräber, M., Hescheler, J., Smyth, N., and Schneider, T. (2002). Disturbances in glucose-tolerance, insulin-release, and stress-induced hyperglycemia upon disruption of the Cav2.3 (α1E) subunit of voltage-gated Ca2+ channels. Mol. Endocrinol. *16*, 884–895.

Quade, B., Camacho, M., Zhao, X., Orlando, M., Trimbuch, T., Xu, J., Li, W., Nicastro, D., Rosenmund, C., and Rizo, J. (2019). Membrane bridging by Munc13-1 is crucial for neurotransmitter release. Elife *8*, e42806.

Rebola, N., Reva, M., Kirizs, T., Szoboszlay, M., Lőrincz, A., Moneron, G., Nusser, Z., and DiGregorio, D.A. (2019). Distinct nanoscale calcium channel and synaptic vesicle topographies contribute to the diversity of synaptic function. Neuron *104*, 693–710.e9.

Reddy-Alla, S., Böhme, M.A., Reynolds, E., Beis, C., Grasskamp, A.T., Mampell, M.M., Maglione, M., Jusyte, M., Rey, U., Babikir, H., et al. (2017). Stable positioning of Unc13 restricts synaptic vesicle fusion to defined release sites to promote synchronous neurotransmission. Neuron *95*, 1350–1364.e12.

Richmond, J.E., Davis, W.S., and Jorgensen, E.M. (1999). UNC-13 is required for synaptic vesicle fusion in *C. elegans*. Nat. Neurosci. *2*, 959–964.

Rosenmund, C., and Stevens, C.F. (1996). Definition of the readily releasable pool of vesicles at hippocampal synapses. Neuron *16*, 1197–1207.

Sakamoto, H., Ariyoshi, T., Kimpara, N., Sugao, K., Taiko, I., Takikawa, K., Asanuma, D., Namiki, S., and Hirose, K. (2018). Synaptic weight set by Munc13-1 supramolecular assemblies. Nat. Neurosci. *21*, 41–49.

Schikorski, T., and Stevens, C.F. (2001). Morphological correlates of functionally defined synaptic vesicle populations. Nat. Neurosci. *4*, 391–395.

Schneider, R., Hosy, E., Kohl, J., Klueva, J., Choquet, D., Thomas, U., Voigt, A., and Heine, M. (2015). Mobility of calcium channels in the presynaptic membrane. Neuron *86*, 672–679.

Schoch, S., Castillo, P.E., Jo, T., Mukherjee, K., Geppert, M., Wang, Y., Schmitz, F., Malenka, R.C., and Südhof, T.C. (2002). RIM1alpha forms a protein scaffold for regulating neurotransmitter release at the active zone. Nature *415*, 321–326.

Schoch, S., Deák, F., Königstorfer, A., Mozhayeva, M., Sara, Y., Südhof, T.C., and Kavalali, E.T. (2001). SNARE function analyzed in synaptobrevin/VAMP knockout mice. Science *294*, 1117–1122.

Siksou, L., Varoqueaux, F., Pascual, O., Triller, A., Brose, N., and Marty, S. (2009). A common molecular basis for membrane docking and functional priming of synaptic vesicles. Eur. J. Neurosci. *30*, 49–56.

Spangler, S.A., Schmitz, S.K., Kevenaar, J.T., de Graaff, E., de Wit, H., Demmers, J., Toonen, R.F., and Hoogenraad, C.C. (2013). Liprin-alpha2 promotes the presynaptic recruitment and turnover of RIM1/CASK to facilitate synaptic transmission. J. Cell Biol. *201*, 915–928.

Sternberg, S.R. (1983). Biomedical image processing. Computer. Long Beach Calif. *16*, 22–34.

Sudhof, T.C. (2004). The synaptic vesicle cycle. Annu. Rev. Neurosci. *27*, 509–547.

Südhof, T.C. (2012). The presynaptic active zone. Neuron *75*, 11–25.

Sun, J., and Roy, S. (2021). Gene-based therapies for neurodegenerative diseases. Nat. Neurosci. *24*, 297–311.

Tang, A.-H., Chen, H., Li, T.P., Metzbower, S.R., MacGillavry, H.D., and Blanpied, T.A. (2016). A trans-synaptic nanocolumn aligns neurotransmitter release to receptors. Nature *536*, 210–214.

Thevenon, J., Callier, P., Andrieux, J., Delobel, B., David, A., Sukno, S., Minot, D., Mosca Anne, L., Marle, N., Sanlaville, D., et al. (2013). 12p13.33 microdeletion including ELKS/ERC1, a new locus associated with childhood apraxia of speech. Eur. J. Hum. Genet. *21*, 82–88.

Todorov, B., van de Ven, R.C.G., Kaja, S., Broos, L.A.M., Verbeek, S.J., Plomp, J.J., Ferrari, M.D., Frants, R.R., and van den Maagdenberg, A.M.J.M. (2006). Conditional inactivation of the Cacna1a gene in transgenic mice. Genesis *44*, 589–594.

Tucker, W.C., Weber, T., and Chapman, E.R. (2004). Reconstitution of Ca2+-regulated membrane fusion by synaptotagmin and SNAREs. Science *304*, 435–438.

Varoqueaux, F., Sigler, A., Rhee, J.S., Brose, N., Enk, C., Reim, K., and Rosenmund, C. (2002). Total arrest of spontaneous and evoked synaptic transmission but normal synaptogenesis in the absence of Munc13-mediated vesicle priming. Proc. Natl. Acad. Sci. USA *99*, 9037–9042.

Verhage, M., and Sørensen, J.B. (2020). SNAREopathies: diversity in mechanisms and symptoms. Neuron *107*, 22–37.

Wang, S.S.H., Held, R.G., Wong, M.Y., Liu, C., Karakhanyan, A., and Kaeser, P.S. (2016). Fusion competent synaptic vesicles persist upon active zone disruption and loss of vesicle docking. Neuron *91*, 777–791.

Wang, Y., Okamoto, M., Schmitz, F., Hofmann, K., and Südhof, T.C. (1997). Rim is a putative Rab3 effector in regulating synaptic-vesicle fusion. Nature *388*, 593–598.

Wong, M.Y., Liu, C., Wang, S.S.H., Roquas, A.C.F., Fowler, S.C., and Kaeser, P.S. (2018). Liprin-α3 controls vesicle docking and exocytosis at the active zone of hippocampal synapses. Proc. Natl. Acad. Sci. USA *115*, 2234–2239.

Wu, L.G., Westenbroek, R.E., Borst, J.G., Catterall, W.A., and Sakmann, B. (1999). Calcium channel types with distinct presynaptic localization couple differentially to transmitter release in single calyx-type synapses. J. Neurosci. *19*, 726–736.

Wu, X., Cai, Q., Shen, Z., Chen, X., Zeng, M., Du, S., and Zhang, M. (2019). RIM and RIM-BP form presynaptic active-zone-like condensates via phase separation. Mol. Cell *73*, 971–984.e5.

Wu, X., Ganzella, M., Zhou, J., Zhu, S., Jahn, R., and Zhang, M. (2021). Vesicle tethering on the surface of phase-separated active zone condensates. Mol. Cell *81*, 13–24.e7.

Wu, Z., Yang, H., and Colosi, P. (2010). Effect of genome size on AAV vector packaging. Mol. Ther. *18*, 80–86.

Zarebidaki, F., Camacho, M., Brockmann, M.M., Trimbuch, T., Herman, M.A., and Rosenmund, C. (2020). Disentangling the roles of RIM and Munc13 in synaptic vesicle localization and neurotransmission. J. Neurosci. *40*, 9372–9385.

Zhen, M., and Jin, Y. (1999). The liprin protein SYD-2 regulates the differentiation of presynaptic termini in *C. elegans*. Nature *401*, 371–375.

Zucker, R.S., and Regehr, W.G. (2002). Short-term synaptic plasticity. Annu. Rev. Physiol. *64*, 355–405.

STAR★METHODS

KEY RESOURCES TABLE

REAGENT or RESOURCE	SOURCE	IDENTIFIER
Antibodies		
guinea pig anti-Bassoon (lab antibody code (LAC): A67)	Synaptic Systems	Cat#: 141 004; RRID: AB_2290619
mouse anti-β-actin (LAC: A127)	Sigma-Aldrich	Cat#: A1978; RRID: AB_476692
rabbit anti-Ca_V2.1 (LAC: A46)	Synaptic Systems	Cat#: 152 203; RRID: AB_2619841
mouse anti-Ca_Vβ4 (LAC: A123)	UC Davis/NIH Neuromab	Cat#: 73-054; RRID: AB_10671176
rabbit anti-ELKSα (LAC: A55)	Abcam	Cat#: ab50312; RRID: AB_869944
rabbit anti-ELKS2α (LAC: A136)	(Held et al., 2016)	E3-1029
rabbit anti-ELKS2αB (LAC: A143)	Abcam	Cat#: ab27250; RRID: AB_731499
rabbit anti-GFP (LAC: A146)	(Han et al., 2004), gift from Dr. T.C. Südhof	RRID: AB_2636878, T3743
rabbit anti-GFP (LAC: A211)	MBL International	Cat#: MBL_598; RRID: AB_591816
mouse anti-HA (LAC: A12)	Biolegend	Cat#: 901501; RRID: AB_2565006
rabbit anti-Liprin-α3 (LAC: A35)	(Schoch et al., 2002), gift from Dr. T.C. Südhof	RRID: AB_2617056, 4396
mouse anti-Map2 (LAC: A108)	Sigma-Aldrich	Cat#: M4403; RRID: AB_477193
rabbit anti-MAP2 (LAC: A139)	Synaptic Systems	Cat#: 188 002; RRID: AB_2138183
rabbit anti-Munc13-1 (LAC: A72)	Synaptic Systems	Cat#: 126 103; RRID: AB_887733
mouse anti-PSD-95 (LAC: A149)	UC Davis/NIH Neuromab	Cat#: 73-028; RRID: AB_10698024
rabbit anti-RIM1 (LAC: A58)	Synaptic Systems	Cat#: 140 003; RRID: AB_887774
rabbit anti-RIM1-Zn (LAC: A148)	(Kaeser et al., 2008), gift from Dr. T.C. Südhof	Q703
rabbit anti-RIM-BP2 (LAC: A126)	Synaptic Systems	Cat#: 316 103; RRID: AB_2619739
mouse anti-Synapsin-1 (LAC: A57)	Synaptic Systems	Cat#: 106 001; RRID: AB_2617071
guinea pig anti-Synaptophysin (LAC: A106)	Synaptic Systems	Cat#: 101 004; RRID: AB_1210382
rabbit anti-Synaptophysin (LAC: A64)	Synaptic Systems	Cat#: 101 002; RRID: AB_887905
goat anti-guinea pig Alexa Fluor 488 (LAC: S3)	Thermo Fisher	Cat#: A11073; RRID: AB_2534117
goat anti-rabbit Alexa Fluor 488 (LAC: S5)	Thermo Fisher	Cat#: A-11034; RRID: AB_2576217
goat anti-mouse IgG1 Alexa Fluor 488 (LAC: S7)	Thermo Fisher	Cat#: A-21121; RRID: AB_2535764
goat anti-mouse IgG1 Alexa Fluor 546 (LAC: S12)	Thermo Fisher	Cat#: A-21123; RRID: AB_2535765
goat anti-rabbit Alexa Fluor 546 (LAC: S16)	Thermo Fisher	Cat#: A-11035; RRID: AB_2534093
goat anti-mouse IgG2a Alexa Fluor 555 (LAC: S20)	Thermo Fisher	Cat#: A-21137; RRID: AB_2535776

(*Continued on next page*)

Continued

REAGENT or RESOURCE	SOURCE	IDENTIFIER
goat anti-guinea pig Alexa Fluor 633 (LAC: S34)	Thermo Fisher	Cat#: A-21105; RRID: AB_2535757
goat anti-mouse peroxidase-conjugated (LAC: S52)	MP Biologicals	Cat#: 0855550; RRID: AB_2334540
goat anti-rabbit peroxidase-conjugated (LAC: S53)	MP Biologicals	Cat#: 0855676; RRID: AB_2334589
Chemicals, Peptides, and Recombinant Proteins		
Picrotoxin	Tocris Bioscience	Cat#: 1128
6-Cyano-7-nitroquinoxaline-2,3-dione (CNQX)	Tocris Bioscience	Cat#: 0190
D-amino-5-phosphonopentanoic acid (D-AP5)	Tocris Bioscience	Cat#: 0106
L-amino-5-phosphonopentanoic acid (L-AP5)	Tocris Bioscience	Cat#: 0107
QX314-Cl	Tocris Bioscience	Cat#: 2313
Tetrodotoxin (TTX)	Tocris Bioscience	Cat#: 1078
Experimental Models: Cell Lines		
HEK293T cells	ATCC	Cat#: CRL-3216; RRID: CVCL_0063
Experimental Models: Organisms/Strains		
Mouse: STOCK *Rims1*^{tm3Sud}/J	(Kaeser et al., 2008)	RRID: IMSR_JAX:015832
Mouse: STOCK *Rims2*$^{tm1.1Sud}$/J	(Kaeser et al., 2011)	RRID: IMSR_JAX:015833
Mouse: STOCK *Erc1*$^{tm2.1Sud}$/J	(Liu et al., 2014)	RRID: IMSR_JAX:015830
Mouse: STOCK *Erc2*$^{tm1.2Sud}$/J	(Kaeser et al., 2009)	RRID: IMSR_JAX:015831
Mouse: Cacna1a conditional knockout	(Todorov et al., 2006)	N/A
Mouse: Cacna1b conditional knockout, Cacna1b$^{tm1a(KOMP)Wtsi}$	(Held et al., 2020)	Cat# KOMP: CSD34514; RRID: IMSR_KOMP: CSD34514-1a-Wtsi
Mouse: Cacna1e conditional knockout	(Pereverzev et al., 2002)	N/A
Recombinant DNA		
pcDNA Ca_V α2δ1 (lab plasmid code (LPC): p752)	Addgene, (Lin et al., 2004)	Cat#: 26575; RRID: Addgene_26575
pCMV β4-Zn-mVenus (LPC: p910)	This paper	N/A
pCMV Cerulean-Ca_V2.1 (LPC: p773)	This paper	N/A
pcDNA Munc13-1-tdTomato (LPC: p888)	(Emperador-Melero et al., 2021)	N/A
pFSW EGFP Δcre (LPC: p010)	(Liu et al., 2014)	N/A
pFSW EGFP cre (LPC: p009)	(Liu et al., 2014)	N/A
pFUGW RIM1α-HA (LPC: p591)	(de Jong et al., 2018)	N/A
pFSW RIM1α-HA (LPC: p592)	This paper	N/A
pFSW HA-ELKS1αB (LPC: p311)	(Nyitrai et al, 2020)	N/A
pFSW HA-ELKS2αB (LPC: p314)	This paper	N/A
pFSW RIM1-Zn-HA (LPC: p654)	This paper	N/A
pFSW RIM1-PDZ-HA (LPC: p648)	This paper	N/A
pFSW RIM1-C_2B-HA (LPC: p647)	This paper	N/A
pFSW RIM1-ΔZn-HA (LPC: p640)	This paper	N/A
pFSW RIM1-ΔPDZ-HA (LPC: p639)	This paper	N/A
pFSW RIM1-ΔC_2A-HA (LPC: p637)	This paper	N/A
pFSW RIM1-ΔC_2B-HA (LPC: p638)	This paper	N/A
pFSW Ca_Vβ4-HA (LPC: p757)	This paper	N/A
pFSW β1b-Zn-HA (LPC: p659)	This paper	N/A

(*Continued on next page*)

Continued

REAGENT or RESOURCE	SOURCE	IDENTIFIER
pFSW β3-Zn-HA (LPC: p660)	This paper	N/A
pFSW β4-Zn-HA (LPC: p661)	This paper	N/A
pFSW Zn-HA-Ca_V2.1 (LPC: p662)	This paper	N/A
pFSW HA-Ca_V2.1-Zn (LPC: p664)	This paper	N/A
pFSW Zn-HA-ELKS2αB (LPC: p657)	This paper	N/A
pFSW HA-Zn-Liprin-α3 (LPC: p658)	This paper	N/A
pFSW Zn-HA-PDZ (LPC: p656)	This paper	N/A
pFSW β4-Zn(K144/146E)-HA (LPC: p898)	This paper	N/A
pFSW Tom20-Cerulean (LPC: p049. mitoC)	(Nyitrai et al., 2020)	N/A
pFSW Tom20-Cerulean-Zn (LPC: p666, mitoC-Zn)	This paper	N/A
pFSW mito-DsRed2 (LPC: p057)	(Nyitrai et al., 2020)	N/A
Software and Algorithms		
Fiji/ImageJ	NIH	RRID: SCR_002285, https://imagej.net/software/fiji/downloads
Prism	GraphPad	RRID: SCR_002798, https://www.graphpad.com/
pClamp	Molecular Devices	RRID: SCR_011323; https://www.moleculardevices.com/products/software/pclamp.html
MATLAB	MathWorks	RRID: SCR_001622, https://www.mathworks.com/products/matlab.html

RESOURCE AVAILABILITY

Lead contact

Further information and requests for resources and reagents should be directed to and will be fulfilled by the lead contact, Pascal S. Kaeser (kaeser@hms.harvard.edu).

Materials availability

Plasmids generated for this study will be shared without restrictions. Antibodies made in the Kaeser laboratory are exhaustible and will be shared as long as they are available. Mouse lines will be shared upon request within the limits of the respective material transfer agreements.

Data and code availability

This study did not generate code. Data reported in this paper are available from the lead contact upon reasonable request. Any additional information required to reanalyze the data reported in this paper is available from the lead contact upon request.

EXPERIMENTAL MODEL AND SUBJECT DETAILS

Animals

The quadruple homozygote floxed mice for RIM1αβ (Kaeser et al., 2008) (RRID: IMSR_JAX:015832, for ablation of the *Rims1* gene to remove RIM1α and RIM1β), RIM2αβγ (Kaeser et al., 2011) (RRID: IMSR_JAX:015833, for ablation of the *Rims2* gene to remove RIM2α, RIM2β and RIM2γ), ELKS1α (Liu et al., 2014) (RRID: IMSR_JAX:015830, for ablation of the *Erc1* gene to remove ELKS1αA and ELKS1αB) and ELKS2α (Kaeser et al., 2009) (RRID: IMSR_JAX:015831, for ablation of the *Erc2* gene to remove ELKS2αA and ELKS2αB) were previously described (Wang et al., 2016). Ca_V2 conditional triple homozygote floxed mice for Ca_V2.1 (Todorov et al., 2006), Ca_V2.2 (Held et al., 2020), and Ca_V2.3 (Pereverzev et al., 2002) mice were previously described (Held et al., 2020). The genotype of all mice was homozygote floxed for the corresponding alleles. Mice were housed as breeding pairs or separated by sex (up to 5 adult mice per cage) in a 12 h light-dark cycle with free access to food and water, in a room dedicated to mouse breeding set to 22 °C (range 20-24 °C) and 50% humidity (range 35-70%). Experiments were performed on cultured primary neurons from postnatal day 0 male and female newborns of these mice. All animal experiments were performed according to institutional guidelines at Harvard University.

Primary cultures

Primary mouse hippocampal cultures were generated from newborn mice as described before (Held et al., 2020; Wang et al., 2016), and cells from mice of both sexes were mixed. Within 24 h after birth, mice were anesthetized on ice slurry, euthanized by decapitation, and the hippocampi were dissected out. Cells were dissociated and plated onto glass coverslips in tissue culture medium composed of Minimum Essential Medium (MEM) with 0.5% glucose, 0.02% $NaHCO_3$, 0.1 mg/mL transferrin, 10% Fetal Select bovine serum (Atlas Biologicals FS-0500-AD), 2 mM L-glutamine, and 25 μg/mL insulin. Cultures were maintained in a 37 °C-tissue culture incubator, and after ~24 h the plating medium was exchanged with growth medium composed of MEM with 0.5% glucose, 0.02% $NaHCO_3$, 0.1 mg/mL transferrin, 5% Fetal Select bovine serum (Atlas Biologicals FS-0500-AD), 2% B-27 supplement (Thermo Fisher 17504044), and 0.5 mM L-glutamine. Around DIV3, depending on growth, 50% or 75% of the medium were exchanged with growth medium supplemented with 4 μM Cytosine β-D-arabinofuranoside (AraC) to inhibit glial cell growth. Analyses were performed at DIV15-19 as described below.

Cell lines

HEK293T cells, an immortalized cell line of female origin, were purchased from ATCC (CRL-3216, RRID: CVCL_0063), expanded, and stored in liquid nitrogen until use. After thawing, the cells were grown in Dulbecco's Modified Eagle Medium (DMEM) with 10% Fetal bovine serum (Atlas Biologicals F-0500-D) and 1% Penicillin-Streptomycin. HEK293T cells were passaged every 2-3 d at a ratio of 1:5 to 1:7. HEK293T cell batches were typically replaced after 20 passages by thawing a fresh vial from the expanded stock.

METHOD DETAILS

Lentiviruses

Lentiviruses were used to transduce primary hippocampal neurons. Lentiviruses expressing EGFP-tagged cre recombinase (to generate cKO^{R+E} neurons, made using pFSW EGFP cre) or a truncated, enzymatically inactive EGFP-tagged cre protein (to generate $control^{R+E}$ neurons, made using pFSW EGFP Δcre) were produced in HEK293T cells by Ca^{2+} phosphate transfection. Protein expression from these lentiviruses was driven by a human synapsin promoter to restrict expression to neurons (Liu et al., 2014; Wang et al., 2016) except for the RIM1α_{high} condition (which was done using FUGW RIM1α-HA with a ubiquitin promoter). For cre-expressing and control virus, neurons were infected with HEK cell supernatant at DIV5 as described (Liu et al., 2014; Wang et al., 2016). For expression of various proteins (ELKS1αB, ELKS2αB, RIM1α, RIM1 mutants, Ca_Vβ4, β4-Zn, mitoC, mitoC-Zn and other RIM1-Zn fusion constructs), neurons were infected with lentivirus for expression of these proteins at DIV3 (a virus made using pFSW without a cDNA inserted in the multiple cloning site was used in the control conditions instead of an expression virus) and with cre or Δcre virus at DIV5 unless noted otherwise. For experiments with Ca_V2 ablation, neurons were infected with cre or Δcre virus at DIV1 and with Ca_Vβ4-expressing virus at DIV3. For experiments with mitoC and mitoC-Zn expression in neurons, neurons were also infected with a lentivirus expressing mito-DsRed at DIV7 to label mitochondria.

Rescue and other constructs

For full-length RIM1α (all residue numbering is according to Uniprot ID Q9JIR4), the open reading frame was subcloned into lentiviral backbones and expression was driven by either a synapsin promoter (pFSW RIM1α-HA, p592) for lower expression or a ubiquitin promoter (pFUGW RIM1α-HA, p591, described in de Jong et al. [2018]) for higher expression. The synapsin promoter was used in all other rescue constructs. For all experiments, RIM zinc finger refers to residues (in single letter code) M1-D213, RIM PDZ to H597-R705, RIM C_2A to Q754-Q882, and RIM C_2B to G1447-S1615. All RIM1 individual domains (pFSW RIM1-Zn-HA, p654; pFSW RIM1-PDZ-HA, p648; pFSW RIM1-C2B-HA, p647) and domain deletion mutants (pFSW RIM1-ΔZn-HA, p640; pFSW RIM1-ΔPDZ-HA, p639; pFSW RIM1-ΔC2A-HA, p637; pFSW RIM1-ΔC2B-HA, p638) span or lack these residues, except for the pFSW RIM1-ΔZn-HA, which spans H597-S1615. In RIM1α and in domain deletion mutants, an HA-tag was inserted between residues E1379-S1380. In RIM1 individual domains, an HA-tag was inserted at the C-terminus. The splice variant of full-length RIM1α was lacking alternatively spliced exons (N83-W105, H1084-R1169, A1207-T1378) identical to previous experiments (Deng et al., 2011; de Jong et al., 2018; Kaeser et al., 2011; Tang et al., 2016). For pFSW HA-ELKS1αB (p311) and pFSW HA-ELKS2αB (p314), an HA-tag was inserted at the N-terminus (Held et al., 2016; Nyitrai et al., 2020). The plasmids for expression of zinc finger fusion proteins were newly generated based on the following cDNAs: pMT2 Ca_Vβ1b GFP (gift from Annette Dolphin obtained through Addgene, plasmid # 89893; http://addgene.org/89893; RRID:Addgene_89893 [Page et al., 2016]), Cavβ3 (gift from Diane Lipscombe; http://addgene.org/26574 RRID:Addgene_26574) and pMT2 Ca_Vβ4 (gift from Annette Dolphin obtained through Addgene, plasmid # 107426; http://addgene.org/107426; RRID:Addgene_107426 [Page et al., 2016]). The cDNAs of Liprin-α3 (Wong et al., 2018), Ca_V2.1 (Held et al., 2020) and RIM1-$Zn^{K144/146E}$ (Deng et al., 2011) were described before. For pFSW β4-Zn-HA (p661), an HA-tag followed by RIM1-Zn was inserted at the C-terminus of Ca_Vβ4, with the stop codon in Ca_Vβ4 and start codon in RIM1-Zn deleted. For all other RIM1-Zn fusion proteins, similar strategies were used as shown in Figure S5A. For pFSW Tom20-Cerulean-Zn (p666, termed mitoC-Zn), a mito-tag composed of the transmembrane domain of the mitochondrial Tom20 protein (Kanaji et al., 2000) and a Cerulean fluorescent protein (pFSW Tom20-Cerulean, p049 (Nyitrai et al., 2020), termed mitoC) was fused onto the N-terminus of RIM1-Zn.

STED imaging

Neurons cultured on 0.17 mm thick 12 mm diameter (#1.5) coverslips were washed two times with warm PBS, and then fixed in 4% PFA for 10 min unless noted otherwise. For $Ca_V2.1$ staining, cultures were fixed in 2% PFA + 4% sucrose (in PBS) for 10 min. After fixation, coverslips were rinsed twice in PBS + 50 mM glycine, then permeabilized in PBS + 0.1% Triton X-100 + 3% BSA (TBP) for 1 h. Primary antibodies were diluted in TBP and stained for 24-48 h at 4 °C. The following primary antibodies were used: guinea pig anti-Synaptophysin (1:500, RRID: AB_1210382, A106), mouse anti-PSD-95 (1:200, RRID: AB_10698024, A149, knockout-verified according to vendor), rabbit anti-RIM1 (1:500, RRID: AB_887774, A58, knockout-verified in lab), rabbit anti-ELKS2α (serum E3-1029, 1:100, custom made, A136, (Held et al., 2016), knockout-verified in lab), rabbit anti-Munc13-1 (1:500, RRID: AB_887733, A72, knockout-verified in lab), rabbit anti-$Ca_V2.1$ (1:200, RRID: AB_2619841, A46, knockout-verified in lab), rabbit anti-RIM-BP2 (1:500, RRID: AB_2619739, A126, knockout-verified in lab), rabbit anti-Liprin-α3 (serum 4396, 1:2000, gift from Dr. T. Südhof, A35, knockout-verified in lab), rabbit anti-Synaptophysin (1:500, RRID: AB_887905, A64), guinea pig anti-$Bassoon^C$ (C-terminal, 1:500, RRID: AB_2290619, A67) and mouse anti-HA (1:500, RRID: AB_2565006, A12, verified in the absence of antigen in lab). After primary antibody staining, coverslips were rinsed twice and washed 3-4 times for 5 min in TBP. Alexa Fluor 488 (anti-guinea pig, RRID: AB_2534117, S3; anti-rabbit, RRID: AB_2576217, S5; anti-mouse IgG1, RRID: AB_2535764, S7), 555 (anti-mouse IgG2a, RRID: AB_1500824, S20), and 633 (anti-rabbit, RRID: AB_2535731, S33; anti-guinea pig, RRID: AB_2535757, S34) conjugated antibodies were used as secondary antibodies at 1:200 (Alexa Fluor 488 and 555) or 1:500 (Alexa Fluor 633) dilution in TBP, incubated for 24 h at 4 °C followed by rinsing two times and washing 3-4 times 5 min in TBP. Stained coverslips were post-fixed for 10 min with 4% PFA in PBS (for $Ca_V2.1$ staining, 4% PFA + 4% sucrose in PBS was used for post-fixation), rinsed two times in PBS + 50 mM glycine and once in deionized water, and air-dried and mounted on glass slides. STED images were acquired with a Leica SP8 Confocal/STED 3X microscope with an oil immersion 100x 1.44 numerical aperture objective and gated detectors as described in Wong et al. (2018); 46.51 x 46.51 μm^2 areas were acquired (4096 x 4096 pixels, 11.358 nm/pixel). Alexa Fluor 633, Alexa Fluor 555, and Alexa Fluor 488 were excited with 633 nm, 555 nm and 488 nm using a white light laser at 2-5% of 1.5 mW laser power. The Alexa Fluor 633 channel was acquired first in confocal mode using 2x frame averaging. Subsequently, Alexa Fluor 555 and Alexa Fluor 488 channels were acquired in STED mode, depleted with 660 nm (50% of max power, 30% axial depletion) and 592 nm (80% of max power, 30% axial depletion) depletion lasers, respectively. Line accumulation (2-10x) and frame averaging (2x) were applied during STED scanning. Identical settings were applied to all samples within an experiment. Synapses within STED images were selected in side-view, defined as synapses that contained a synaptic vesicle cluster labeled with Synaptophysin and associated with an elongated PSD-95 structure along the edge of the vesicle cluster as described (Held et al., 2020; de Jong et al., 2018; Nyitrai et al., 2020; Wong et al., 2018). For intensity profile analyses, side-view synapses were selected using only the PSD-95 signal and the vesicle signal for all experiments. An ROI was manually drawn around the PSD-95 signal and fit with an ellipse to determine the center position and orientation. A ~1200 nm long, 200nm wide rectangle was then selected perpendicular and across the center of the elongated PSD-95 structure. Intensity profiles were obtained for all three channels within this ROI. To align individual profiles, the PSD-95 signal only was smoothened using a moving average of 5 pixels, and the smoothened signal was used to define the peak position of PSD-95. All three channels (vesicle marker, test protein, and smoothened PSD-95) were then aligned to the PSD-95 peak position and averaged across images. Analyses were performed on raw images without background subtraction, and adjustments were made identically for all experimental conditions. Here (Figure S2) and in previous analyses (Wong et al., 2018), levels analyzed with STED microscopy correlate well with those analyzed in confocal microscopy despite the non-linearities that may be present in these methods. Representative images in figures were brightness and contrast adjusted to facilitate inspection, and these adjustments were made identically for images within an experiment. The experimenter was blind to the condition/genotype for image acquisition and analyses.

Confocal imaging of cultured neurons

Neurons cultured on glass coverslips were washed with warm PBS and fixed in 4% PFA for 20 min. Neurons were permeabilized in TBP for 1 h, and then incubated in primary antibodies at 4 °C overnight. The following primary antibodies were used: rabbit anti-RIM1 (1:1000, RRID: AB_887774, A58, knockout-verified in lab), rabbit anti-ELKSα (1:500, RRID: AB_869944, A55, knockout-verified in lab), rabbit anti-Munc13-1 (1:500, RRID: AB_887733, A72, knockout-verified in lab), rabbit anti-$Ca_V2.1$ (1:1000, RRID: AB_2619841, A46, knockout-verified in lab), rabbit anti-RIM-BP2 (1:500, RRID: AB_2619739, A126, knockout-verified in lab), mouse anti-Bassoon (1:500, RRID: AB_11181058, A85), mouse anti-MAP2 (1:500, RRID: AB_477193, A108), rabbit anti-MAP2 (1:1000, RRID: AB_2138183, A139), guinea pig anti-Synaptophysin (1:500, RRID: AB_1210382, A106), rabbit anti-GFP (1:500, RRID: AB_591816, A211, verified in the absence of antigen in lab). After staining with primary antibodies, coverslips were rinsed twice and washed 3-4 times for 5 min in TBP. Alexa Fluor 488 (for detection of the protein of interest, anti-rabbit, RRID: AB_2576217, S5; anti-mouse IgG1, RRID: AB_2535764, S7), 546 (for detection of MAP2, anti-mouse IgG, RRID: AB_2535765, S12; anti-rabbit, RRID: AB_2534093, S16), and 633 (for detection of Synaptophysin, anti-guinea pig, RRID: AB_2535757, S34) conjugated secondary antibodies were used at 1:500 dilution in TBP. Secondary antibody staining was done for 2 h at room temperature followed by rinsing two times and washing 3-4 times 5 min in TBP. Coverslips were rinsed once with deionized water and mounted on glass slides. Images were taken on an Olympus FV1200 confocal microscope with a 60x oil-immersion objective or on a Leica SP8 Confocal/STED 3X microscope with a 63x oil-immersion objective using identical settings per condition in a given experiment and single confocal sections were analyzed in ImageJ. For quantitative analyses of synaptic protein levels and mitochondrial Munc13-1 levels, the Synaptophysin- or DsRed-signals were used to define ROIs, respectively. The signal intensity of the protein of interest was quantified

within these ROIs. For each image, the ''rolling ball'' ImageJ plugin was set to a diameter of 1.4 μm for local background subtraction (Sternberg, 1983). Representative images in figures were brightness and contrast adjusted to facilitate inspection, and adjustments were made identically across conditions. The experimenter was blind to the condition/genotype for image acquisition and analyses.

Confocal imaging in transfected HEK293T cells

For confocal analyses of $Ca_V2.1$, β4-Zn and Munc13-1 staining in HEK293T cells, cells were plated on matrigel-coated glass coverslips (12 mm in diameter) at 10-20% confluency in 12-well plates. 24 h later, cells were co-transfected with pcDNA α2δ1 (p752), pCMV β4-Zn-mVenus (p910) and pcDNA Munc13-1-tdTomato (p888) with or without pCMV Cerulean-$Ca_V2.1$ (p773) at 1:1:1(:1) molar ratio with a total of 347 (500 ng) of DNA per well per well. 24 h after transfection, the cells were washed with warm PBS and fixed in 4% PFA in PBS for 10 min. Coverslips were rinsed once with deionized water and mounted onto glass slides for imaging of fluorophores without additional staining. Images were taken using identical settings per condition on a Leica SP8 Confocal/STED 3X microscope with a 63x oil-immersion objective and single confocal sections were analyzed in ImageJ. Based on the localization of Cerulean-$Ca_V2.1$, a 1 μm-thick ROI was set along the outer edge of the cell (edge), and the enclosed area was defined as the inside of the cell (inside). The average intensity within the edge ROI and inside ROI was quantified and the edge:inside ratio was calculated for each cell. Representative images in figures were brightness and contrast adjusted to facilitate inspection, and these adjustments were made identically for images within an experiment. The experimenter was blind to the condition for image acquisition and analyses.

Electrophysiology

Electrophysiological recordings in cultured hippocampal neurons were performed as described (Held et al., 2020; Liu et al., 2014; Wang et al., 2016) at DIV15-19. Glass pipettes were pulled at 2 - 5 MΩ and filled with intracellular solutions containing (in mM) for EPSC recordings: 120 Cs-methanesulfonate, 2 $MgCl_2$, 10 EGTA, 4 Na_2-ATP, 1 Na-GTP, 4 QX314-Cl, 10 HEPES-CsOH (pH 7.4, ~300 mOsm) and for IPSC recordings: 40 CsCl, 90 K-gluconate, 1.8 NaCl, 1.7 $MgCl_2$, 3.5 KCl, 0.05 EGTA, 2 Mg-ATP, 0.4 Na_2-GTP, 10 phosphocreatine, 4 QX314-Cl, 10 HEPES-CsOH (pH 7.2, ~300 mOsm). Cells were held at +40 mV for NMDAR-EPSC recordings and at -70 mV for AMPAR-EPSC, mEPSC, sucrose EPSC, IPSC and sucrose IPSC recordings. Access resistance was monitored during recordings and compensated to 3-5 MΩ, and cells were discarded if the uncompensated access exceeded 15 MΩ. The extracellular solution contained (in mM): 140 NaCl, 5 KCl, 2 $MgCl_2$, 1.5 $CaCl_2$, 10 glucose, 10 HEPES-NaOH (pH 7.4, ~300 mOsm), the $CaCl_2$ concentration was 0.5 mM instead of 1.5 mM for Figures S3A–S3D, all recordings were performed at room temperature (20-24 °C). To assess action potential-triggered excitatory transmission, NMDAR-mediated excitatory postsynaptic currents (NMDAR-EPSCs) were measured to avoid network activity induced by AMPA receptor activation unless noted otherwise. For NMDAR-EPSCs, picrotoxin (PTX, 50 μM) and 6-Cyano-7-nitroquinoxaline-2,3-dione (CNQX, 20 μM) were present in the extracellular solution, for Figures S3E–S3H, 20 μM L-AP5 was added to the extracellular solution. For AMPAR-EPSCs, D-amino-5-phosphonopentanoic acid (D-APV, 50 μM) and PTX (50 μM) were present in the extracellular solution; 1 mM γ-D-Glutamylglycine (γ-DGG) was also added to the bath to prevent AMPAR saturation, which also reduced the reverberant activity that is present upon electrical stimulation. Inhibitory postsynaptic currents (IPSCs) were recorded in the presence of D-APV (50 μM) and CNQX (20 μM) in the extracellular solution. Action potentials were elicited with a bipolar focal stimulation electrode fabricated from nichrome wire. Paired pulse ratios were calculated as the amplitude of the second PSC divided by the amplitude of the first at each interval from an average of 6 sweeps per cell and interval. The baseline value for the second PSC was taken immediately after the second stimulus artifact. For dependence of IPSC amplitudes on the extracellular Ca^{2+} concentration ($[Ca^{2+}]_{ex}$), neurons were perfused with solutions containing 0.5/3.5, 1/3, 2/2, 5/0.25, 10/0.25 mM $[Ca^{2+}]_{ex}$/$[Mg^{2+}]_{ex}$ in variable order. Recordings began at 0.5 mM $[Ca^{2+}]_{ex}$/3.5 mM $[Mg^{2+}]_{ex}$ and for each solution exchange, five chamber volumes of solution were replaced. Only cells in which all five $[Ca^{2+}]_{ex}$ were recorded were included in the analysis. For the normalized data, IPSC amplitudes for each cell were normalized to the same cell's amplitude at 10 mM $[Ca^{2+}]_{ex}$/0.25 mM $[Mg^{2+}]_{ex}$. The absolute and normalized data were fit to the Hill equation $I = I_{min} + ([Ca^{2+}]_{ex}\text{^HillSlope}) * (I_{max} - I_{min}) / ([Ca^{2+}]_{ex}\text{^HillSlope} + EC_{50}\text{^HillSlope})$. For EGTA-dependence of IPSCs, 100 μM EGTA-AM in DMSO (final DMSO 0.33% of total volume), or DMSO only as control, was added to the media and the neurons were incubated for 10 min in a 37 °C tissue culture incubator. The neurons were then transferred from culture medium to extracellular solution and recorded as described above. For normalization, four to five cells incubated with DMSO only were recorded for each genotype in each culture, and the IPSCs in EGTA-AM were normalized to the average of these control cells per genotype and culture. For mEPSC recordings and sucrose-induced EPSC recordings, TTX (1 μM), PTX (50 μM), and D-APV (50 μM) were added to the extracellular solution, and for sucrose-induced IPSC recordings, TTX (1 μM), CNQX (20 μM), and D-APV (50 μM) were added. mEPSC were identified with a template search followed by manual confirmation by an experimenter, and their frequencies were assessed during a 100-s recording time window after stabilizing the baseline for 3-min after break-in. mEPSC amplitudes and mEPSC kinetics were determined for each cell by averaging the waveform of all events identified during the 100-s recording time window aligned to the beginning of the events. Rise times were measured as the time interval between 20% and 80% of the peak amplitude and decay τ as the interval from 100% to 37% of the decay phase. The RRP was estimated by application of 500 mM sucrose in extracellular solution applied via a microinjector syringe pump for 10 s at a rate of 10 μl/min through a tip with an inner diameter of 250 μm. For sucrose concentration-dependence, solutions with 250 mM, 500 mM or 1000 mM sucrose (in extracellular solution) were used. Data were acquired at 5 kHz and lowpass

filtered at 2 kHz with an Axon 700B Multiclamp amplifier and digitized with a Digidata 1440A digitizer. All data acquisition and analyses were done using pClamp10. For electrophysiological experiments, the experimenter was blind to the genotype throughout data acquisition and analysis.

High-pressure freezing and electron microscopy

Neurons cultured on 6 mm matrigel-coated sapphire coverslips were frozen using a Leica EM ICE high-pressure freezer in extracellular solution containing (in mM): 140 NaCl, 5 KCl, 2 $MgCl_2$, 2 $CaCl_2$, 10 HEPES-NaOH (pH 7.4), 10 Glucose (~300 mOsm) with CNQX (20 μM), D-AP5 (50 μM) and PTX (50 μM) added to block synaptic transmission. After freezing, samples were first freeze-substituted (AFS2, Leica) in 1% glutaraldehyde, 1% osmium tetroxide, 1% water in anhydrous acetone as follows: -90 °C for 5 h, 5 °C per h to -20 °C, -20 °C for 12 h, and 10 °C per h to 20 °C. Following freeze substitution, samples were Epon infiltrated, and baked for 48 h at 60 °C followed by 80 °C overnight before sectioning at 50 nm. For ultrathin sectioning, the sapphire coverslip was removed from the resin block by plunging the sample first in liquid nitrogen and followed by warm water several times until the sapphire was completely detached. The resin block containing the neurons was then divided into four pieces, and one piece was mounted for sectioning. Ultrathin sectioning was performed on a Leica EM UC7 ultramicrotome, and the 50 nm sections were collected on a nickel slot grid (2 x 1 mm) with a carbon coated formvar support film. The samples were counterstained by incubating the grids with 2% lead acetate solution for 10 s, followed by rinsing with distilled water. Images were taken with a transmission electron microscope (JEOL 1200 EX at 80 kV accelerating voltage) and processed with ImageJ. The total number of vesicles, the distance of individual vesicles to the active zone area of the presynaptic membrane (defined by apposition to the PSD), the number of docked vesicles per synapse profile, the length of the PSD, and the area of the presynaptic bouton were analyzed in each section using a custom-written Matlab code. Bouton size was calculated from the measured perimeter of each synapse. Docked vesicles per active zone were defined as vesicles touching the presynaptic plasma membrane opposed to the PSD, and only vesicles for which the electron densities of the vesicular membrane and the presynaptic plasma membrane merged such that they were not separated by less electron dense space were considered docked. We also measured vesicle distribution within 100 nm from the presynaptic membrane in 10 nm bins. Across experiments, vesicle distributions in 0−10 nm were altered within the first 100 nm depending on genotype/manipulation, largely reflecting changes in docked vesicles as defined above. We show vesicle distribution as an inset for the first electron microscopic experiment (Figure 2B), but only report docked vesicles for subsequent experiments for simplicity. Due to the laborious nature of these experiments, it was not possible to include a RIM1α full-length rescue condition in each experiment. Instead, we always included control^{R+E} and cKO^{R+E} neurons as essential controls for comparison. For assessment of vesicles tethered to mitochondria, the number of small vesicles (diameter < 50 nm) associated with the mitochondrial surface was counted. A vesicle was considered tethered if it was within 70 nm from a mitochondrial surface, as this was the longest tether that we visually identified previously (Nyitrai et al., 2020). The number of vesicles was normalized to the mitochondrial perimeter (μm) for each mitochondrion. Experiments and analyses were performed by an experimenter blind to the genotype.

Western blotting

For assessment of rescue protein expression in cultured neurons, Western blotting was used to detect target proteins in cell lysates from select coverslips of every culture that was used for electrophysiology or electron microscopy. At DIV15-19, cultured neurons were harvested in 20 μl 1x SDS buffer per coverslip and run on standard SDS-Page gels followed by transfer onto nitrocellulose membranes. Membranes were blocked in filtered 10% nonfat milk/5% goat serum for 1 h at room temperature and incubated with primary antibodies in 5% nonfat milk/2.5% goat serum overnight at 4 °C, and HRP-conjugated secondary antibodies (1:10,000, anti-mouse, RRID: AB_2334540; anti-rabbit, RRID: AB_2334589) were used. Anti-Synapsin or -β-actin antibodies were used as loading controls. The following primary antibodies were used: rabbit anti-RIM1 (1:1000, RRID: AB_887774, A58, knockout-verified in lab), rabbit anti-ELKS2αB (1:500, RRID: AB_731499, A143, knockout-verified in lab), rabbit anti-RIM1-Zn (1:500, gift from Dr T. Südhof, A148, knockout-verified in lab), mouse anti-HA (1:1000, RRID: AB_2565006, A12, verified in the absence of antigen in lab), mouse anti-Synapsin (1:4000, RRID: AB_2617071, A57, knockout-verified according to vendor), rabbit anti-GFP (1:2000, RRID:AB_2636878, A146, verified in the absence of antigen in lab), mouse anti-β-actin (1:2000, RRID: AB_476692, A127), mouse anti-Ca_Vβ4 (1:50, RRID: AB_10671176, A123). For illustration in figures, images were adjusted for brightness and contrast to facilitate visual inspection.

QUANTIFICATION AND STATISTICAL ANALYSIS

Data are displayed as mean ± SEM. Statistics were performed in GraphPad Prism 9, and significance is presented as * $P < 0.05$, ** $P < 0.01$, and *** $P < 0.001$. Sample sizes and statistical tests for each experiment are included in each figure legend. For electrophysiological experiments, the sample size used for statistical analyses was the number of recorded cells. For STED microscopic and electron microscopic data, the sample size used for statistical analyses was the number of synapses except for Figures 8I–8K, where it was the number of mitochondria. For confocal microscopic data, the sample size used for statistical analyses was the number of analyzed ROIs, which corresponds to the number of images (Figures 8F–8H and S2A–S2F) or the number of cells (Figures 8A–8E). Parametric tests were used for normally distributed data (assessed by Shapiro-Wilk tests) or when sample size was $n \geq 30$. One-way ANOVA, followed by Dunnett's multiple comparisons post-hoc tests, was used

for datasets with equal variance. When variances were unequal, Welch's unequal variances t-test, Brown-Forsythe ANOVA followed by Games-Howell's multiple comparisons post hoc tests (for $n \geq 50$) or Dunnett's T3 multiple comparisons post hoc tests (for $n < 50$) were used. For non-normally distributed data, nonparametric tests were used (Mann-Whitney tests or Kruskal-Wallis tests followed by Dunn's multiple comparisons post-hoc tests). For paired pulse ratios, two-way ANOVA with Dunnett's tests was used. For STED side-view analyses, two-way ANOVA with Dunnett's tests was used on a 200 nm-window centered around the active zone peak. For each dataset, the specific tests used are stated in the figure legends.

Neuron, Volume *110*

Supplemental information

Rebuilding essential active zone functions within a synapse

Chao Tan, Shan Shan H. Wang, Giovanni de Nola, and Pascal S. Kaeser

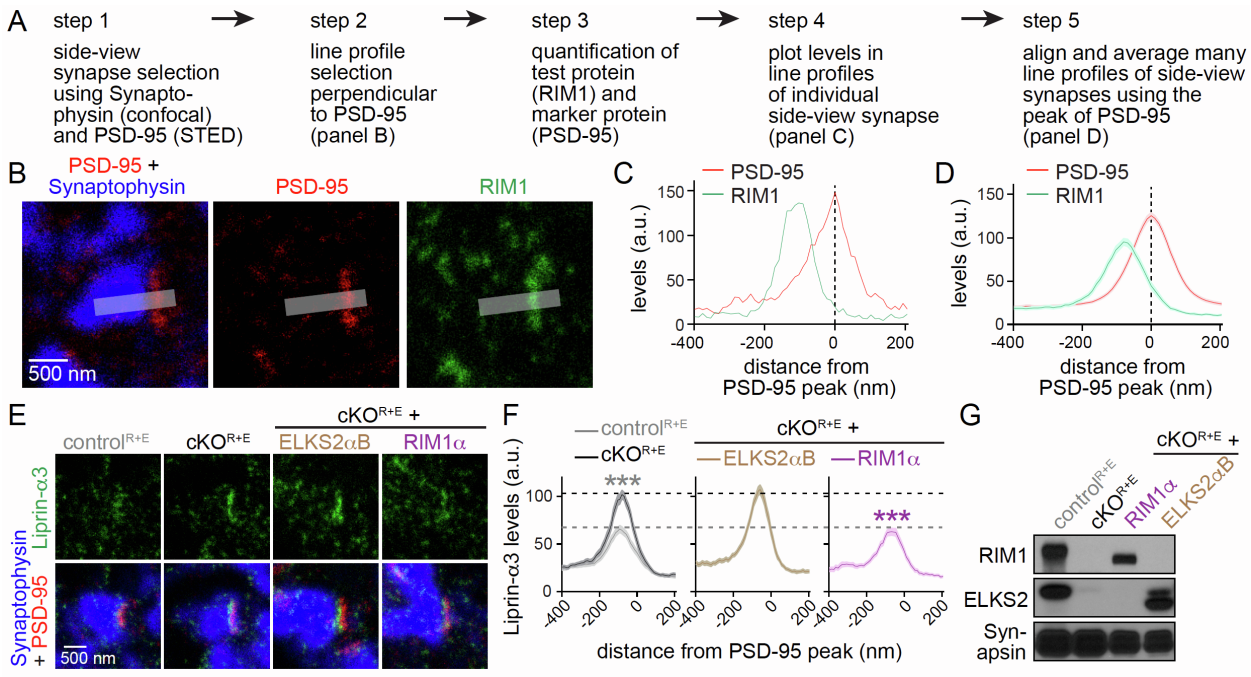

Figure S1. Workflow of STED analyses and additional assessment of protein expression and localization, related to Figure 1

(**A**) Workflow for STED side-view synapse analyses as described previously (Held et al., 2020; Nyitrai et al., 2020).

(**B**) Example STED images of a side-view synapse (the control^{R+E} images shown in Fig. 1B are reproduced here) stained for PSD-95 (STED), RIM1 (STED) and Synaptophysin (confocal).

(**C**) Quantification of fluorescent signals of PSD-95 and RIM1 labeling of the synapse shown in B.

(**D**) Summary data of a full experiment for PSD-95 and RIM1, these are the same data as the control^{R+E} data shown in Fig. 1C.

(**E, F**) Sample STED images (E) and quantification (F) of side-view synapses stained for Liprin-α3 (STED), PSD-95 (STED), and Synaptophysin (confocal) of control^{R+E} and cKO^{R+E} neurons, and of cKO^{R+E} neurons after re-expression of ELKS2αB or RIM1α, dotted lines mark control^{R+E} (grey) and cKO^{R+E} (black) levels for comparison, 60 synapses/3 cultures each.

(**G**) Western blot for RIM1, ELKS2 and Synapsin in homogenates of control^{R+E} and cKO^{R+E}

neurons, and of cKO^{R+E} neurons after re-expression of the main active zone isoforms of each protein family, ELKS2αB or RIM1α. Rescue proteins were expressed at levels similar to or below wild type proteins. Note the double band in lentivirally expressed but not endogenous ELKS2, which might be due to different post-translational modification of rescue vs. endogenous ELKS2αB, the recognition of alternative start codons in virally expressed ELKS2αB or degradation of virally expressed but not endogenous ELKS2 before or during generation of the homogenates.

Data are mean ± SEM; ***$P < 0.001$ compared to cKO^{R+E} as determined by two-way ANOVA followed by Dunnett's tests (F).

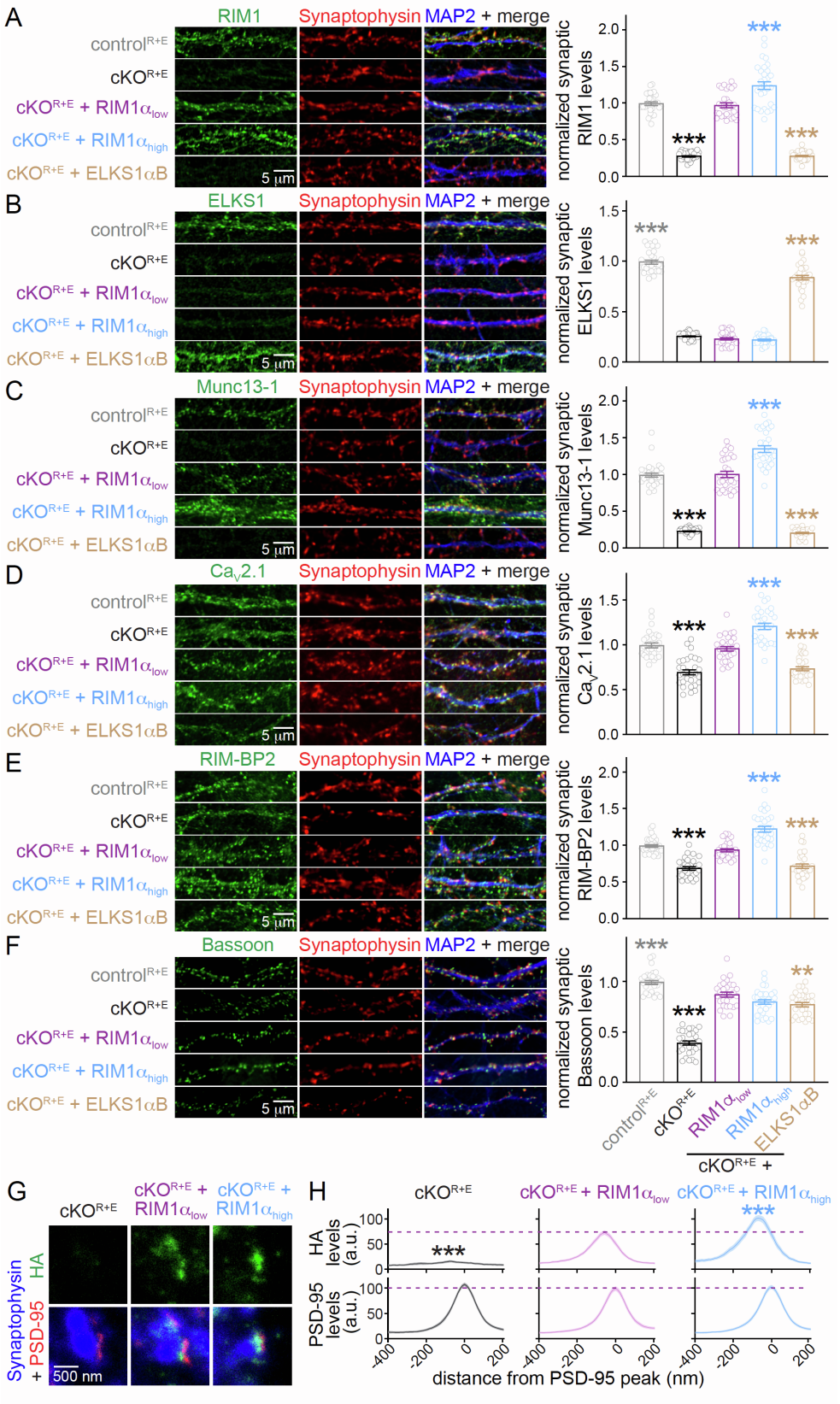

Figure S2. Synaptic RIM1α levels determine levels of interacting active zone proteins,

related to Figure 1

(**A**) Sample confocal images (left) and quantification (right) of RIM1 levels in control^{R+E} and cKO^{R+E} synapses, and in cKO^{R+E} synapses expressing HA-tagged full-length RIM1α or ELKS1αB. Neurons were infected at DIV3 with lentiviruses expressing RIM1α under a synapsin promoter for lower expression (RIM1α$_{low}$), or under a ubiquitin promoter for higher expression (RIM1α$_{high}$). Synaptophysin staining was used to define ROIs, and levels of RIM1 were quantified within those ROIs and normalized in each culture to levels in control^{R+E} neurons, 30 images/3 cultures each.

(**B**-**F**) Same as A, but for ELKS1 (B), Munc13-1 (C), Ca$_V$2.1 (D), RIM-BP2 (E), and Bassoon (F). Note that the levels of Munc13-1, Ca$_V$2.1, and RIM-BP2 correlate well with levels of RIM. In contrast to re-expressed ELKS2αB which does not localize to cKO^{R+E} synapses (Fig. 1), re-expressed ELKS1αB is localized at least in part to synapses and restores some synaptic Bassoon (F). This may be related to distinct functions and differential localization of ELKS proteins, with ELKS2αB at the active zone and ELKS1αB broadly distributed throughout the nerve terminal (Nyitrai et al., 2020), 30/3 each.

(**G, H**) Sample STED images (G) and quantification (H) of side-view synapses stained for HA (STED), PSD-95 (STED), and Synaptophysin (confocal) of cKO^{R+E} neurons, and of cKO^{R+E} neurons after re-expression of HA-tagged full-length RIM1α (RIM1α$_{low}$ and RIM1α$_{high}$ as in A-F), purple dotted lines mark cKO^{R+E} + RIM1α$_{low}$ levels for comparison, 60 synapses/3 cultures each. Data are mean ± SEM; $^{**}P < 0.01$, $^{***}P < 0.001$ compared to cKO^{R+E} + RIM1α$_{low}$ as determined Brown-Forsythe ANOVA followed by Dunnett's T3 test (A, B, C and E), by one-way ANOVA followed by Dunnett's tests (D and F), or by two-way ANOVA followed by Dunnett's tests (H).

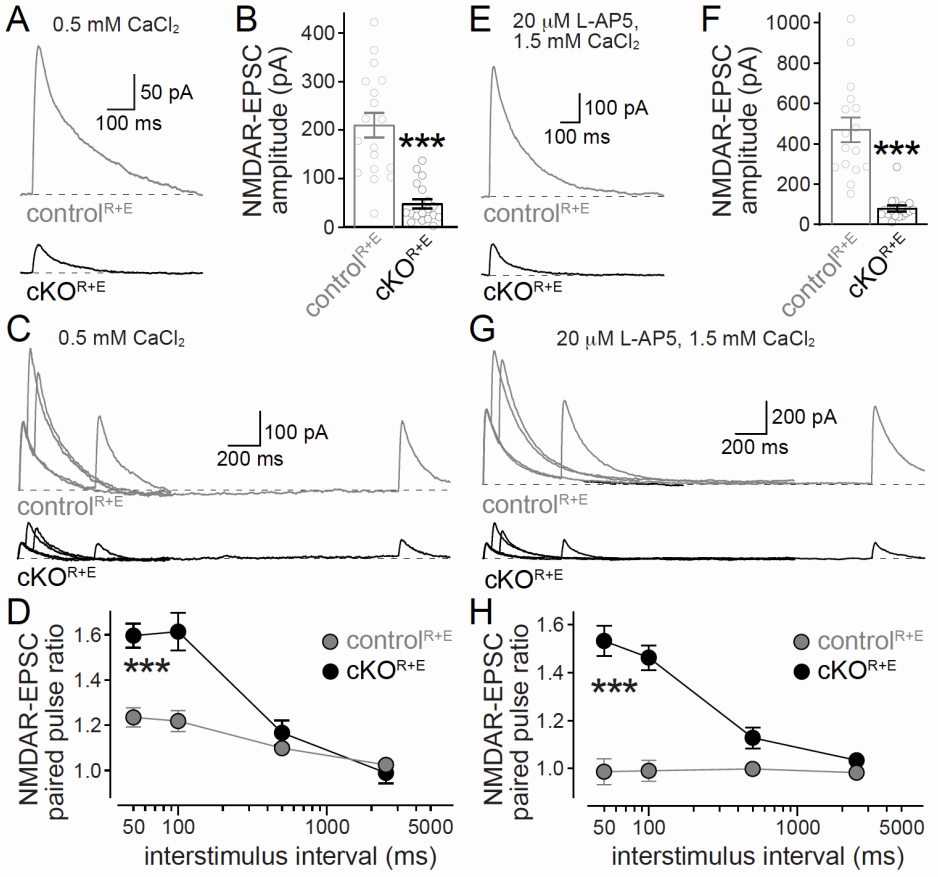

Figure S3. Additional characterization of NMDAR-mediated synaptic transmission, related to Figure 2

(**A, B**) Sample traces (A) and quantification (B) of NMDAR-mediated EPSCs evoked by focal electrical stimulation with 0.5 mM Ca^{2+} in the extracellular solution (instead of 1.5 mM used unless noted otherwise), 18 cells/3 cultures each.

(**C, D**) Sample traces (C) and quantification (D) of NMDAR-mediated paired pulse ratios induced with focal electrical stimulation in extracellular solution containing 0.5 mM Ca^{2+} (instead of 1.5 mM used unless noted otherwise). The relationship of paired pulse ratios between cKO^{R+E} and $control^{R+E}$ was similar in 0.5 (D) or 1.5 mM (Fig. 2H) Ca^{2+}, 16/3 each.

(**E, F**) Sample traces (E) and quantification (F) of NMDAR-mediated EPSCs evoked by focal electrical stimulation in 1.5 mM Ca^{2+} and in the presence of 20 μM of the low affinity NMDAR antagonist L-AP5 to prevent NMDAR saturation, 16/3 each.

(**G, H**) Sample traces (G) and quantification (H) of NMDAR-mediated paired pulse ratios induced with focal electrical stimulation in extracellular solution containing 1.5 mM Ca^{2+} and 20 μM L-AP5. Paired pulse ratios between cKO^{R+E} and $control^{R+E}$ were similar with (H) or without (Fig. 2H) L-AP5, 16/3 each. Overall, A-H indicate that NMDAR saturation does not confound the estimates of p in our standard conditions (1.5 mM Ca^{2+}, no L-AP5).

Data are mean ± SEM; ***$P < 0.001$ compared to $control^{R+E}$ as determined by Mann-Whitney tests (B and F) or two-way ANOVA followed by Dunnett's tests (D and H).

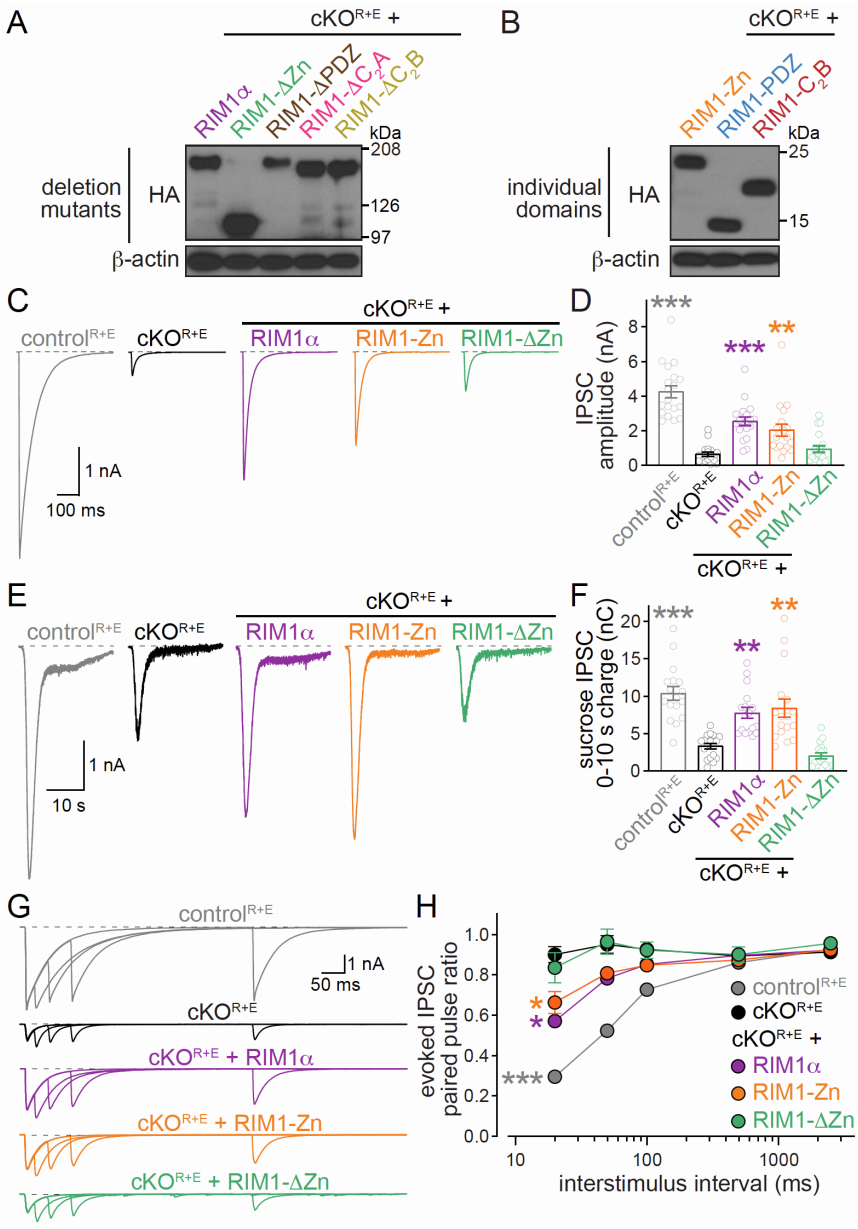

Figure S4. RIM zinc finger re-expression restores the RRP at inhibitory cKO^{R+E} synapses, related to Figures 3 and 4

(**A, B**) Expression levels of rescue constructs used in Fig. 3 were assessed with anti-HA antibodies in homogenates of cultured neurons, and anti-β-actin antibodies were used as loading controls. Several RIM1-C$_2$A constructs were generated, but their expression could not be detected by Western blotting, and constructs were hence not further used for experimentation.

(**C, D**) Sample traces (C) and quantification (D) of IPSCs evoked by focal electrical stimulation, control^{R+E} 19 cells/5 cultures, cKO^{R+E} 19/5, cKO^{R+E} + RIM1α 19/5, cKO^{R+E} + RIM1-Zn 18/5, and cKO^{R+E} + RIM1-ΔZn 19/5.

(**E, F**) Sample traces (E) and quantification (F) of IPSCs triggered by hypertonic sucrose, 17/3 each.

(**G, H**) Sample traces (G) and quantification (H) of IPSC paired pulse ratios, control^{R+E} 17/5, cKO^{R+E} 17/5, cKO^{R+E} + RIM1α 18/5, cKO^{R+E} + RIM1-Zn 17/5, and cKO^{R+E} + RIM1-ΔZn 18/5. Data are mean ± SEM; **P* < 0.05, ***P* < 0.01, ****P* < 0.001 compared to cKO^{R+E} as determined by Kruskal-Wallis tests followed by Dunn's multiple comparisons post-hoc tests (D and F) or two-way ANOVA followed by Dunnett's tests (H).

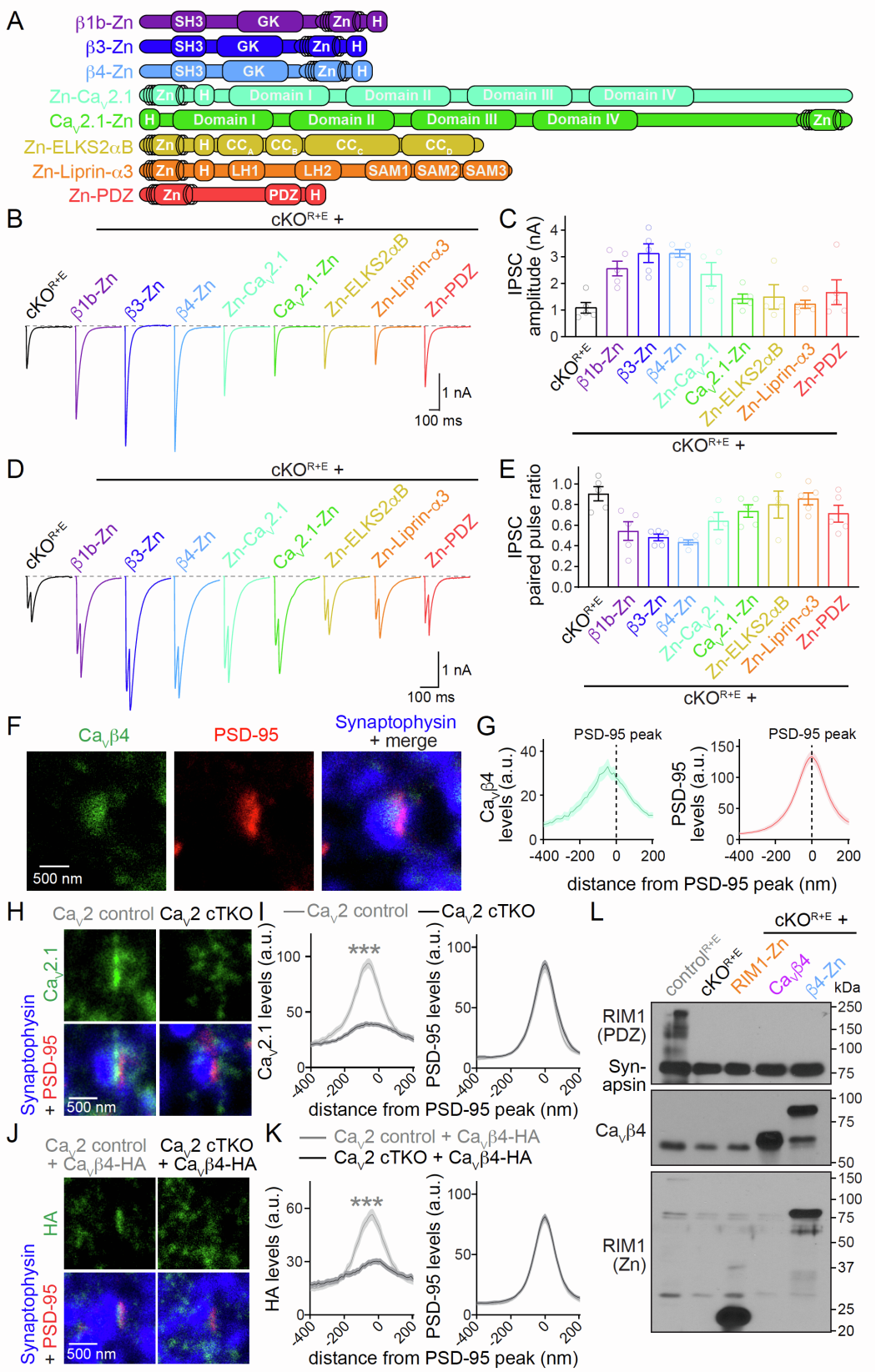

Figure S5. Screening of fusion-proteins for restoring action potential-triggered release at

cKO^{R+E} synapses, related to Figure 5

(**A**) Schematic representation of fusion-proteins of the RIM1 zinc finger domain to Ca_Vβ1b, Ca_Vβ3, Ca_Vβ4, Ca_V2.1 (N- or C-terminal fusions), ELKS2αB, Liprin-α3 or RIM1-PDZ.

(**B, C**) Sample traces (B) and quantification of IPSC amplitudes (C) evoked by focal stimulation, 4-5 cells/1 culture each.

(**D**, **E**) Sample traces (D) and quantification (E) of IPSC paired pulse ratios at 20 ms interstimulus intervals, 4-5 cells/1 culture each.

(**F, G**) Sample STED images (F) and quantification (G) of side-view synapses stained for Ca_Vβ4 (STED), PSD-95 (STED), and Synaptophysin (confocal) in wild type synapses, 23 synapses/1 culture.

(**H, I**) Sample STED images (H) and quantification (I) of side-view synapses stained for Ca_V2.1 (STED), PSD-95 (STED), and Synaptophysin (confocal) in Ca_V2 cTKO and Ca_V2 control neurons generated as described before (Held et al., 2020). Quantification establishes efficient removal of Ca_V2.1 in Ca_V2 cTKO, 63/3 each.

(**J, K**) Sample STED images (J) and quantification (K) of side-view synapses stained for HA (STED), PSD-95 (STED), and Synaptophysin (confocal). Quantification of HA staining establishes that active zone targeting of HA-tagged Ca_Vβ4 necessitates the presence of the pore-forming Ca_V2 α1-subunits, 61/3 each.

(**L**) Expression levels of RIM1 and rescue constructs in homogenates of cultured control^{R+E} and cKO^{R+E} neurons were assessed with anti-RIM1 PDZ (top), anti-Ca_Vβ4 (middle) and anti-RIM1 zinc finger (bottom) antibodies, and anti-Synapsin antibodies were used as loading controls. Data shown as mean ± SEM, ***P < 0.001 compared to Ca_V2 control as determined by two-way ANOVA followed by Dunnett's tests (I and K); no statistics were performed for C, E and G due to the limited number of observations. Based on the apparent rescue activity of β4-Zn for evoked IPSC amplitudes and paired pulse ratios, and the active zone-like localization of Ca_Vβ4 including its dependence on Ca_V2s, β4-Zn was chosen for full characterization.

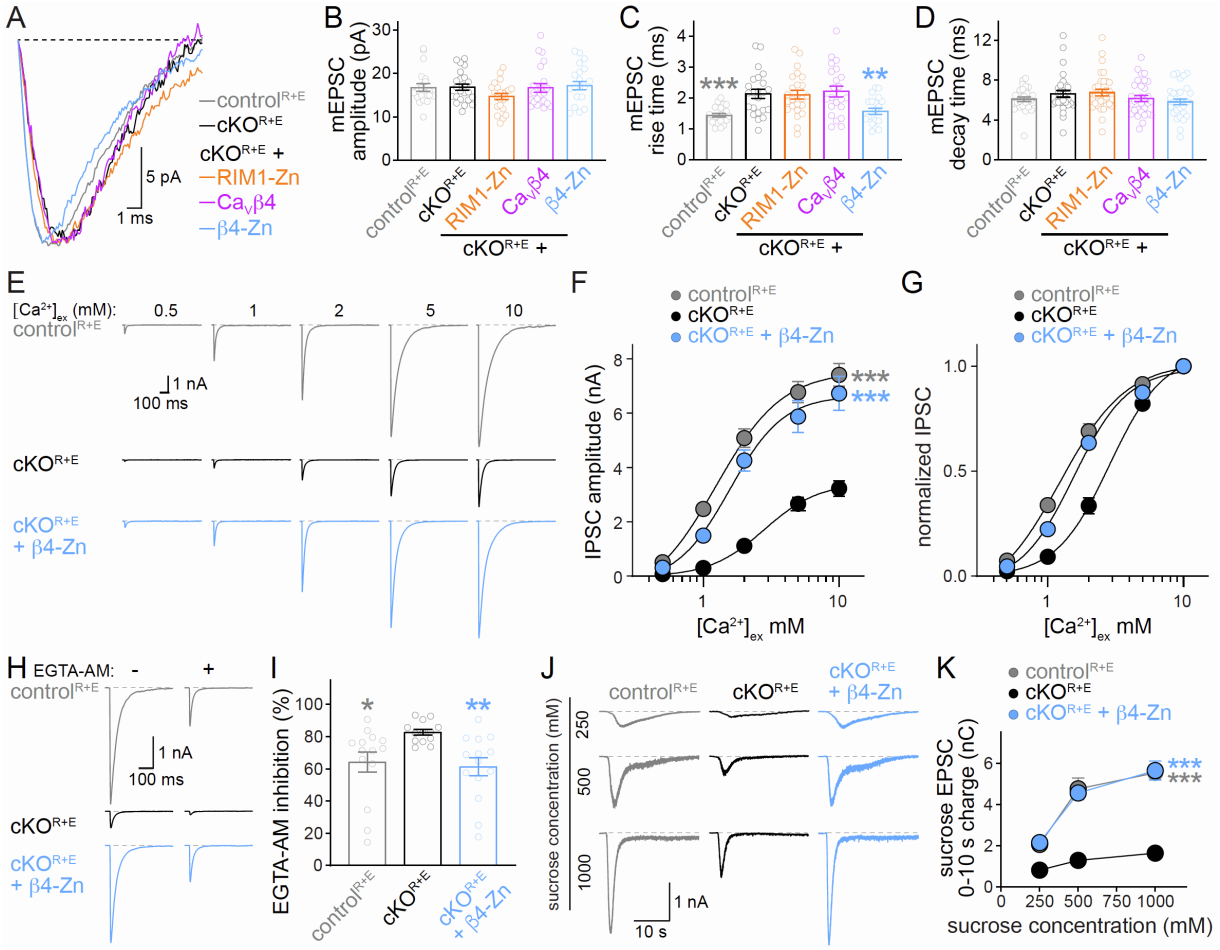

Figure S6. β4-Zn restores vesicle release, related to Figure 6

(**A**) Sample traces of average mEPSCs of a single cell per condition.

(**B-D**) Quantification of mEPSC amplitudes (B), rise times (C, 20%-80%) and decay times (D, τ), control^{R+E} 21/3, cKO^{R+E} 23/3, cKO^{R+E} + RIM1-Zn 23/3, cKO^{R+E} + Ca$_V$β4 22/3, and cKO^{R+E} + β4-Zn 21/3.

(**E-G**) Sample traces (E) and quantification (F, absolute IPSC amplitudes; G, IPSC amplitudes normalized to the IPSC at 10 mM $[Ca^{2+}]_{ex}$) of the extracellular Ca^{2+}-dependence of IPSCs evoked by focal electrical stimulation, control^{R+E} 11/3, cKO^{R+E} 10/3, cKO^{R+E} + β4-Zn 11/3.

(**H**, **I**) Sample traces (H) and quantification (I) of IPSCs recorded with or without a 10-min pre-incubation in 100 µM EGTA-AM, control^{R+E} 14/3, cKO^{R+E} 13/3, cKO^{R+E} + β4-Zn 14/3.

(**J**, **K**) Sample traces (J) and quantification (K) of IPSCs triggered by hypertonic sucrose, 15/3

each (250 mM and 500 mM sucrose) or 16/3 each (1000 mM sucrose).

Data are mean ± SEM; *P < 0.05, **P < 0.01, ***P < 0.001 compared to cKO^{R+E} as determined by Brown-Forsythe ANOVA followed by Dunnett's T3 test (C), Kruskal-Wallis tests followed by Dunn's multiple comparisons post-hoc tests (I), or by two-way ANOVA followed by Dunnett's tests (F and K).

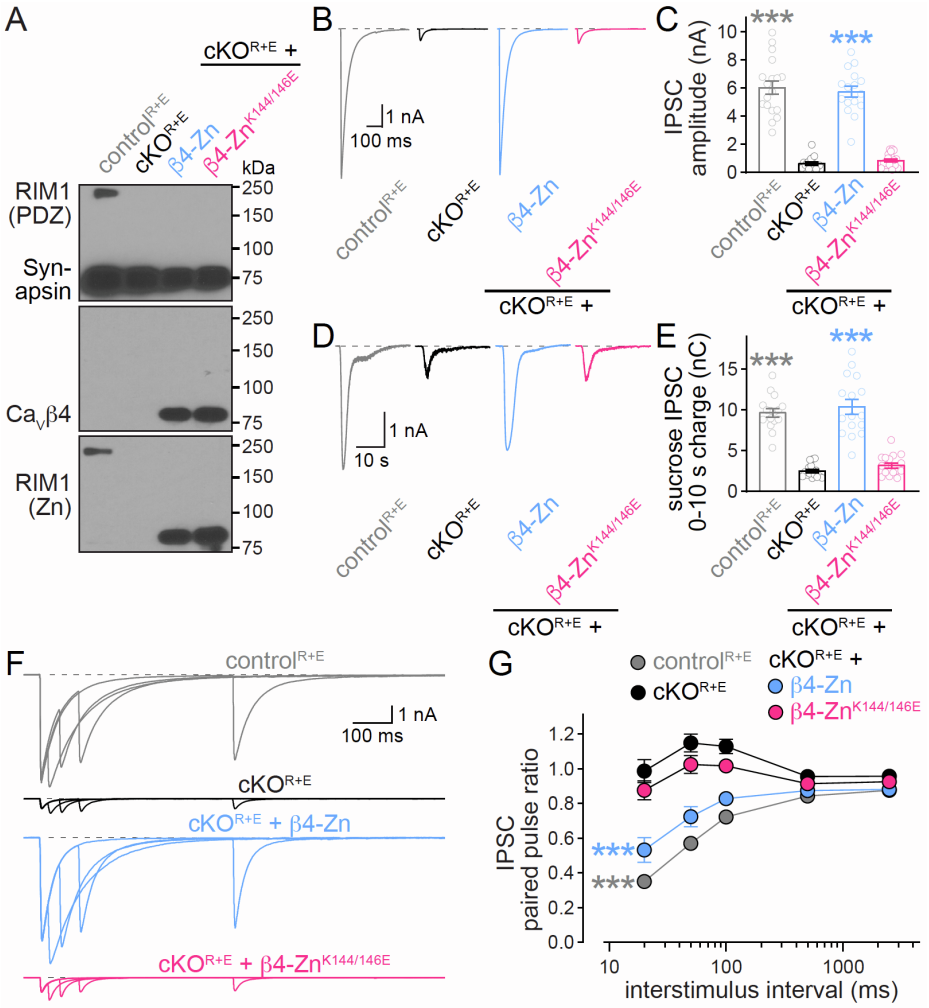

Figure S7. Binding of β4-Zn to Munc13 is essential for restoring release at inhibitory cKO^{R+E} synapses, related to Figure 7

(**A**) Expression levels of RIM1 and rescue constructs in homogenates of cultured control^{R+E} and cKO^{R+E} neurons were assessed with anti-RIM1 PDZ (top), anti-Ca$_V$β4 (middle) and anti-RIM1 zinc finger (bottom) antibodies, and anti-Synapsin antibodies were used as loading controls.

(**B, C**) Sample traces (B) and quantification (C) of IPSCs evoked by focal electrical stimulation, control^{R+E} 18/3, cKO^{R+E} 17/3, cKO^{R+E} + β4-Zn 16/3, and cKO^{R+E} + β4-Zn$^{K144/146E}$ 18/3.

(**D**, **E**) Sample traces (D) and quantification (E) of IPSCs triggered by hypertonic sucrose, 16/3 each.

(**F**, **G**) Sample traces (F) and quantification (G) of IPSC paired pulse ratios, 16/3 each.

Data are mean ± SEM; ***$P < 0.001$ compared to cKO^{R+E} as determined by Kruskal-Wallis tests followed by Dunn's multiple comparisons post-hoc tests (C and E) or by two-way ANOVA followed by Dunnett's tests (G).

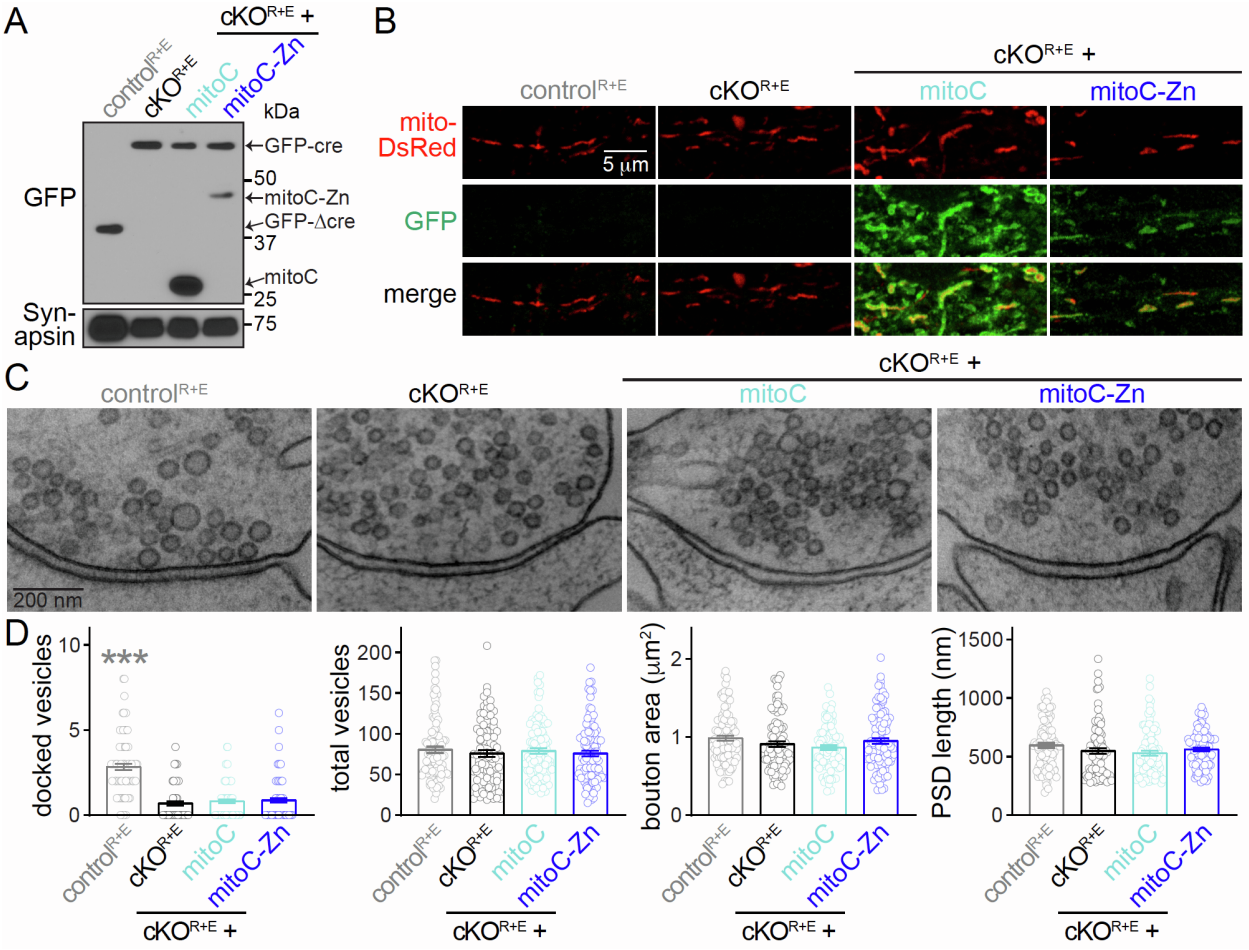

Figure S8. Assessment of protein expression, localization and synapse morphology after targeting of RIM1-Zn to mitochondria, related to Figure 8

(**A**) Expression levels of expressed proteins in cultured control^{R+E} and cKO^{R+E} neurons, and in cKO^{R+E} neurons transduced with lentiviruses expressing either mitoC or mitoC-Zn were assessed with anti-GFP-antibodies, anti-Synapsin antibodies were used as loading controls. Anti-GFP-antibodies detect the GFP-cre and -Δcre fusion proteins, and the mito-Cerulean fusion proteins.

(**B**) Sample confocal images of cultured control^{R+E} and cKO^{R+E} neurons, and of cKO^{R+E} neurons transduced with lentiviruses expressing mitoC or mitoC-Zn. Mitochondria were labeled in all groups with mito-DsRed expression. The culture was stained with anti-GFP antibodies to detect mito-Cerulean fusion proteins; cre- and Δcre-fusion proteins are strictly localized to nuclei,

which are not included in the sample images.

(**C, D**) Sample electron microscopic images (C) and analyses (D) of synapses of high-pressure-frozen neurons, control^{R+E} 96 synapses/2 cultures, cKO^{R+E} 92/2, cKO^{R+E} + mitoC 97/2, and cKO^{R+E} + mitoC-Zn 101/2.

Data are mean ± SEM; ***P < 0.001 compared to cKO^{R+E} as determined by Brown-Forsythe ANOVA followed by Games-Howell's tests (D, docked vesicles).